Soft Embedded Sensors with Learning-based Calibration for Soft Robotics

Tannaz Torkaman

A Thesis

in

The Department

of

Mechanical, Industrial, and Aerospace Engineering

Presented in Partial Fulfillment of the Requirements

for the Degree of

Master of Applied Science (Mechanical Engineering) at

Concordia University

Montréal, Québec, Canada

November 2022

CONCORDIA UNIVERSITY

School of Graduate Studies

This is to certify that the thesis prepared

By: **Tannaz Torkaman**

Entitled: **Soft Embedded Sensors with Learning-based Calibration for Soft Robotics**

and submitted in partial fulfillment of the requirements for the degree of

Master of Applied Science (Mechanical Engineering)

complies with the regulations of this University and meets the accepted standards with respect to originality and quality.

Signed by the Final Examining Committee:

______________________________ Chair
Dr. Ramin Sedaghati

______________________________ External Examiner
Dr. Amin Hammad

______________________________ Examiner
Dr. Ramin Sedaghati

______________________________ Supervisor
Dr. Javad Dargahi

Approved by ______________________________
Martin D. Pugh, Chair
Department of Mechanical, Industrial, and Aerospace Engineering

____________ 2022

____
Mourad Debbabi, Dean
Faculty of Engineering and Computer Science

Abstract

Soft Embedded Sensors with Learning-based Calibration for Soft Robotics

Tannaz Torkaman

In this thesis, a new class of soft embedded sensors was conceptualized and three novel sensors were designed, fabricated, and tested for small force range soft robotic applications. The proposed soft sensors were consisted of a gelatin-graphite composite with piezoresistive characteristics. Principally, the sensing elements of the proposed class of soft sensors were moldable into any shape and size; thus, were embeddable and scalable. The sensing elements were directly molded into soft flexural structures so as to be embedded in the flexures. For each sensor, first a mechano-electrical phenomenological model for the exhibited piezoresistivity was proposed and validated experimentally. Afterwards, the sensors were subjected to a series of external forces to obtain calibration data. Given the complexity of the piezoresistivity and intrinsic large deformation of the soft bodies and sensing element, learning-based calibration approach were investigated. To compensate rate-dependency and hysteresis effects on sensor readings in calibration, rate-dependent features were selected for learning-based calibrations. Consequently, the first sensor of this research, i.e., one degree-of-freedom (1-DoF) force sensor, exhibited a force range of 0.035-0.82 N force measurement range with a mean-absolute-error (MAE) of 3.7% and a resolution of 4% of full-range. The second sensor, i.e., 3-DoF had a measurement range of up to 0.3 N with an MAE of 0.005 N and a resolution of 0.003 N. The third sensor, 6-DoF force-torque sensor, had a force range of up to 110 mN with an MAE of 7.4$\pm$6.5 mN and resolution of 1 mN and a torque range of 6.8 mNm with an MAE of 0.24 mNm. Comparison with the state-of-the-art and functional requirements of intraluminal procedures showed that the the proposed sensors were fairly compatible with the requirement and showed improvement of the state of the art. The major contribution of this research was to proposed a scalable sensing principle that could adapt its shape to the shape of the host body, e.g., flexural robots. Moreover, this research showed nonlinear learning-based calibration is a fitting solution to overcome limitations of the state-of-the-art in using soft elastomeric sensors.

Acknowledgments

I would want to thank my husband, Majid joon, for his unwavering support of my work and this endeavour. Without his overall curiosity about sensors and his input on my writing, I would not have been able to defend my thesis as quickly as I did. I also wished to acknowledge his cooking expertise, which made my contribution to this project considerably more manageable.

In addition, I wanted to recognise my parents' efforts since, if they did not see their name, they would be angry that I had not thanked them for paying my tuition when there was a financing issue.

I would also want to thank my supervisor, Professor Javad Dargahi, for allowing me to join the Surgical Robotic Laboratory and work with its amazing team.

Next, I'd want to express my gratitude to my mentor, Dr. Amir Hooshiar, for his consistent assistance, devoted support, and wise guidance during this research effort. I appreciate that he never gave up on me, despite me providing him with numerous excuses, including my inability to save images in PNG format.

I am grateful to Majid Roshanfar and Amir Sayadi, my colleagues, for addressing all of my inquiries. In addition, Saeed, Negin, Hadis, Foad, Mina, Hooman, Kawan, Sina, and Amir are among the friends and loved ones who have made this journey enjoyable and less stressful.

Finally, I would like to thank my cat Gojo for his loyalty and support. I believe he would not care if he could read my thesis, but at least he knew I would not abandon him at home without a reason.

Contents

List of Figures

List of Tables

Nomenclature

$2D$	Two-dimensional
$3D$	Three-dimensional
ΔV	Voltage variation
$\dot{V}$	Voltage temporal rates
λ	Longitudinal stretch
ϕ	Diameter
ρ	Resistivity
σ	Nominal stress
A	Cross sectional area
Ag	Silver
Au	Gold
Co	Cobalt
CP	Carbon particle
Cu	Copper
DOF	Degree of freedom
dS	Original length of the differential element

ds Deformed length of the differential element

$EGaIn$ Eutectic gallium–indium

F Force

FEM Finite element modeling

FOS Fiber optic sensors

GND Ground

H Hysteresis

Hg Mercury

L Length

MIS Minimally invasive surgery

MR Magnetic resonant

MRI magnetic resonance imaging

$MWNT$ Multi-walled carbon nanotubes

$NaCl$ Sodium chloride

Ni Nickel

NP Nanoparticles

Pd Palladium

$PDMS$ Polydimethylsiloxane

PI Polyimide

PLA Polylactide acid

Pt platinum

PU Polyurethane

R Resistance

$R_\circ$ Initial resistance

R_c Constant resistor

$RMIS$ Robotic-assisted minimally invasive surgery

$RMSE$ root-mean-square error

$TESM$ Triboelectric tactile sensing approaches

V Voltage

$V_\circ$ Pull-up voltage

V_e Voltage in the end of sensing element

V_m Voltage in the middle of sensing element

Chapter 1

Introduction

1.1 Background

1.1.1 Robotic assisted minimally invasive surgery

Studies on medical robotics and biomechatronic systems can be traced back to the 1970s when open surgery began to be replaced. The traditional approach for surgeries, which dates back to the 1600s, includes gaining access to the internal organs through a wide aperture in order to facilitate the safe manipulation of specialized tools and visibility of the processes. To perform surgery on the heart's valves or blood arteries, the typical procedure for cardiac interventions entails a wide chest cavity incision. Thus, patients who undergo open surgery experience pain, infection at the surgical site, excessive blood loss, and lengthy hospital stays after the procedure [1].

Minimally invasive surgery (MIS) became a better alternative to open surgery in the mid-1970s.In contrast to open surgery, minimally invasive surgery (MIS) involves the use of long rigid, or flexible surgical instruments that are inserted into the body through small incisions. The primary objective of MIS is to complete a surgical procedure as safely and quickly as possible while causing the least damage to surrounding tissue. Because of the benefits it can provide in terms of patient safety, patient comfort, healing time, shorter hospitalization, fewer complication rates, and distress, MIS is becoming more popular as an alternative to open surgery [2]. However, due to the inaccessibility of the MIS operating field, surgeons face numerous obstacles when executing their procedures [3].

Figure 1.1: da Vinci robotic surgical system [4]

With the advent of robots in MIS, the precision and dexterity of surgical instrument handling significantly improved [5]. Therefore, as a more accurate procedure, robotically assisted surgery is less likely to result in patient harm [6]. The field of surgical robotics has advanced dramatically over the past four decades, with rapt utilization causing a paradigm change that has had a quantifiable favorable effect on surgical results. In addition, the integration of robotics with minimally invasive surgery (MIS) has led to improved methods for overcoming some constraints of traditional open surgery [1]. However, there is no natural haptic feedback in this procedure because the surgeon no longer manually manipulates the device. Surgeons and robotics researchers believe that the lack of haptic feedback in existing RMIS systems is a significant drawback [5]. The absence of haptic input, which comprises kinesthetic (force) and cutaneous (tactile) feedback, might compromise the surgery's quality [7]. As a result, sensors are an essential part of this procedure. The use of a sensor to measure tactile cues can ultimately improve surgical efficiency by boosting the surgeon's situational awareness [5]. For that reason, Specific physical and functional requirements must be met by sensors. They should be able to be scaled to fit in the required space. The sensor must also perform in both static and dynamic circumstances, which is especially important for moving organs like the heart [8]. Various characteristics, such as the required number of measured degrees of freedom (DOFs) and the location of the sensing device, affect the nature of sensor design problems. While 6-DOF force and torque sensing are ideal, fewer DOFs may be adequate for many applications [9].

Moreover, Sterilization is another important consideration in the design of sensing equipment, particularly those that may be introduced into the human body [10].
In surgical force sensing devices, several measurement approaches have been used, which were developed mainly based on optical or electrical principles [11].

1.1.2 Applications of Tactile Sensors in MIS

At the site of contact between surgical equipment and tissues, tactile sensors are employed to gather tactile data. Various physical qualities (e.g., softness and roughness) of tissue can be derived from tactile data, depending on the modalities of the tactile signal. The surgeons are subsequently provided with tactile input based on the observed physical qualities. In the vast majority of published works, force feedback is the most prevalent type of tactile feedback, and force sensors are the most commonly employed tactile sensors. There are two types of tactile sensors: the single-point tactile sensor and the tactile array sensor [12]. In this section, research on providing force feedback with the two tactile sensors listed above are reviewed.

Single-Point sensor

Typically, a single-point tactile sensor is placed on the tip of surgical equipment to confirm object–sensor contact and detect tactile signals at the point of contact. In minimally invasive surgery (MIS), force feedback is crucial for clinicians to consider the varying consistency of tissue. The force feedback suggests that the active force is immediately applied to the operator's hands, whereas the active force is often associated with the reactive force from the tissue to the tools [12]. Numerous studies examined the various application scenarios of force feedback in MIS:

- knot-tying: The initial factor is the force applied to the tool's tip. This force is particularly valuable for determining the thread's tension. It is crucial to apply the correct amount of tension while tying knots that are strong enough to hold but will not tear sutures or injure tissue [13].

- Incision: The sensor must provide direct sensing of normal and shear forces at surgical instrument tips for the process [14].

- Palpation: During tissue palpation, force feedback helps characterize tissue qualities to locate lumps or tumors [15].

Tactile Array Sensor

A tactile array sensor consists of many single-point tactile sensors arranged in accordance with specified rules. It is often a cuboid with M N tactile sensing units, where M and N represent the number of rows and columns, respectively. In the previous decades, tactile data sensed by a tactile array sensor was typically shown as a wave diagram with M N waveforms, where each waveform represents a time-dependent physical quantity collected by a sensing unit [1].

1.1.3 types of soft sensors in MIS application

RMIS haptic feedback devices are continuously being developed and evaluated. The majority only provide force feedback with poor fidelity. A few tactile feedback systems for RMIS have been developed; however, their clinical viability must be demonstrated [5]. Researchers have examined the physical and functional requirements of tactile sensors for surgical applications from multiple perspectives. Currently, sensors can be identified as optical sensors or electrical sensors, as demonstrated in Fig.1.2.

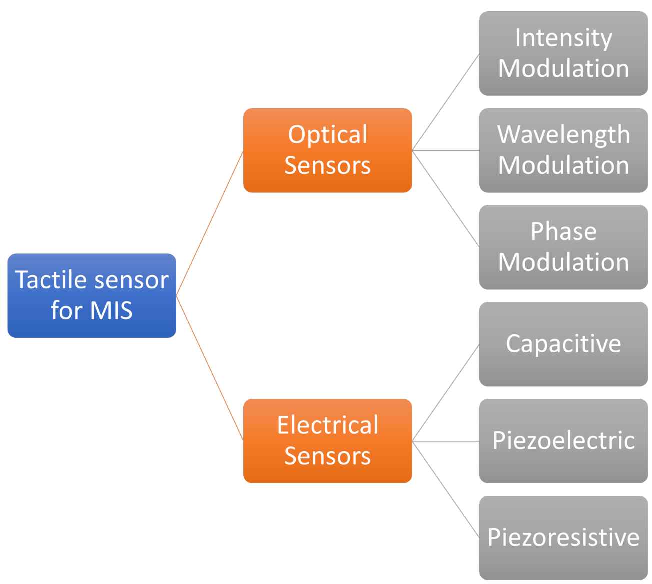

Figure 1.2: Tactile sensor categories proposed for minimally invasive surgery.

Optical Sensors

Fiber optic sensors (FOSs) are increasingly being used in medical equipment and technology. Since the late 1990s, when the first generation of in vivo pressure detection probes was marketed, a significant amount of research has gone into producing a new generation of FOSs [16].

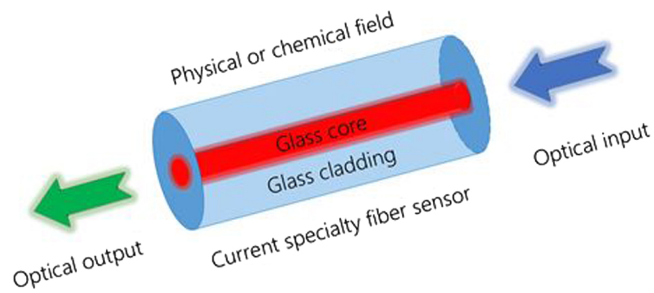

Figure 1.3: Traditional specialty optical fiber sensor schematic [17]

As shown in Fig.1.3, optical fibers are thin, flexible ”wires” constructed of glass or plastic that can transfer light signals over vast distances with low loss. A sensing layer generates light signals. Light is transported through optical fibers to the sensing layer, where it is used to measure the interactions between the analyte and the sensing layer using various optical phenomena [18]. Additionally, utilizing optical fiber technology offers a number of benefits. The sensors are biocompatible and resistant to electromagnetic interference. They can be put non-invasively against external organs or surgically exposed surfaces. Moreover, because of their flexibility, they can be inserted into body cavities [19]. Because of its low hysteresis and high precision detection, the optical sensor technology is a suitable solution. Magnetic resonant (MR) compatibility is an additional advantage of optical fiber sensors. In the medical field, magnetic resonance imaging (MRI) is commonly used to examine living organs [20]. Also, the optical fiber contains no internal sensor circuit reduces the complexity. Although optical fibers have a lot of potential for sensing instrument development, there are several limits to using them. The measurement accuracy of intensity-modulated sensors, in particular, could be decreased if the light signal is altered outside the transduction zone, such as outside the fiber cables and at their connectors, due to bending and misalignments. As a result, methods of avoidance or compensation, such as the use of a reference fiber, must be implemented. Furthermore, many optical fibers are not as flexible as electric lines; they are readily broken and typically require precise connections with other system components. Small fiber bending can cause signal attenuation and fluctuation, which must be adjusted for, but large bending can cause fiber core damage [21]. Moreover, these fiber optic sensors are sensitive to temperature changes and have installation accuracy issues when embedded in soft robots [22].

Electrical Sensors

Electrical-based tactile sensors are the most commonly proposed sensing modality for MIS, and the tactile transduction techniques currently in use are based on capacitive, piezoelectric, piezoresistive, and triboelectric tactile sensing approaches (TESM). Each of these transduction techniques possesses specific properties.

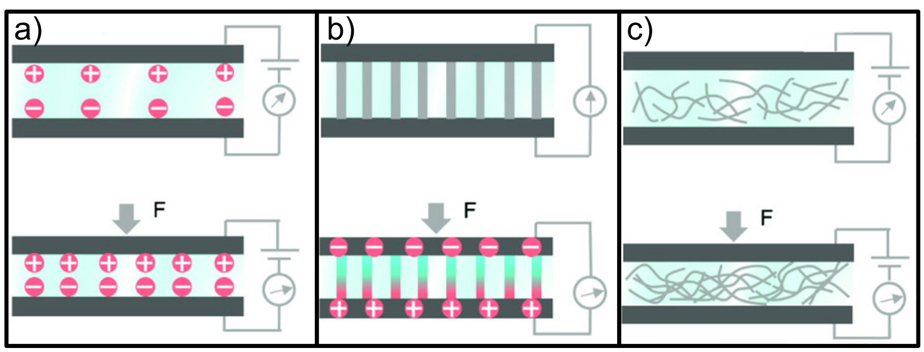

Figure 1.4: Electric sensors' sensing concept a) Capacitive, b) Piezoelectric, and c) Piezoresistive [23].

Capacitive tactile sensing, demonstrated in Fig.1.4 a, is based on analyzing changes in the geometry of a capacitor via changes in its capacitance due to mechanical factors. Two conducting plates are separated by an insulating layer to form a capacitive sensor shown in Fig1.5. By adjusting their relative position with an applied force, the distance between the plates and/or their effective area is altered [24]. Capacitance is the ability of a capacitor to store electrical charge in a broad sense [25]. Low power consumption, temperature independence, and long-term signal stability are all advantages of capacitive tactile sensors. They are, however, extremely susceptible to electromagnetic interference and necessitate a sophisticated measurement circuit [26].

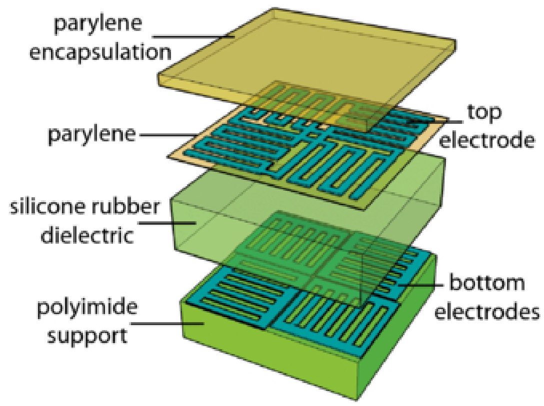

Figure 1.5: Two layers of metallic electrodes are placed in three layers of polymeric packaging to form a flexible capacitive force sensor [27].

Piezoelectricity is the collection of electric charge on the surface of a solid as a result of physical stress. Such charge accumulation on one surface of solid results in an electrical potential difference across the solid. As a result, the distorted solid functions as a capacitor. Yet, as electric charges migrate from high potential to low potential, and in the absence of a physical barrier, such as a dielectric, the charges migrate to low potential sites. Under constant mechanical stress, this causes the piezoelectric effect to be transient (static loading) [11]. Piezoelectric tactile sensors have a high sensitivity and dynamic response, making them good choices for dynamic pressure detection, such as vibration detection and texture characterization. The piezoelectric effect occurs only when the applied stimuli change, which limits the detection of static pressure [26].

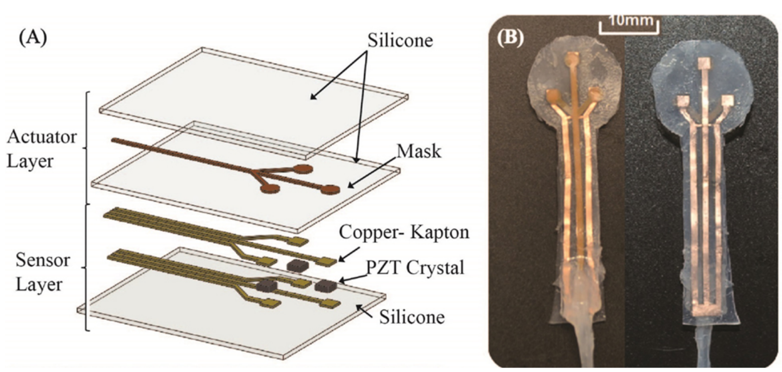

Figure 1.6: the schematic of the multi-layer construction of piezoelectric soft skin [28].

Resistive and piezoresistive strain sensors, in another hand, assess variations in resistance produced by changes in the geometry or resistivity of conducting materials [29]. Resistive tactile sensors are made up of active materials placed between two opposing electrodes or placed on a pair of in-plane electrodes. Active materials are typically composites formed of conductive components and a matrix. When force is exerted on the sensor, the connections with conductive materials in a porous matrix or the surface between the conductive materials and electrodes expand, significantly lowering the resistance. The composition and geometric design of the active material are essential drivers of the tactile sensor's performance because it acts as both an electrical channel for current flow and a flexible structure throughout the operation [26].

1.1.4 Piezoresistive Tactile Sensors

Resistance in sensors was introduced using several approaches. Changes in the dimensions of a piezoresistive sensor due to applied force or pressure will result in changes in its resistivity, which is the working principle of this type of sensor [30]. Several strategies have been proposed to integrate the Piezoresistive sensor with MIS [31]. Bandari et al. [32] gathered the improvements for this approach from the early studies in the area of intravascular neurosurgery when piezoresistive strain gauges were used on silicon. The silicon base enables a better deformation while the resistance in the gauges changes [33]. Later on, gauge strain sensors with the same principle were used to provide haptic feedback for laparoscopy equipment such as grasper. High precision and the safety of the body that is made of silicon rubber are the two significant advantages of this method [34, 35]. The variety of application and fabrication methods paved the way for researchers to introduce more creative designs, whether the goal is to implement the sensor onto a da Vinci robotic system [36] or a catheter-based cardiac surgery [37]. One of the features of a piezoresistive sensor that plays an essential role in robotic surgery is its ability to exhibit an acceptable stretch [38]. While elastomers were previously introduced to soft robots, using a conductive material embedded with the elastomer is the key to creating piezoresistivity for sensing ability [39].

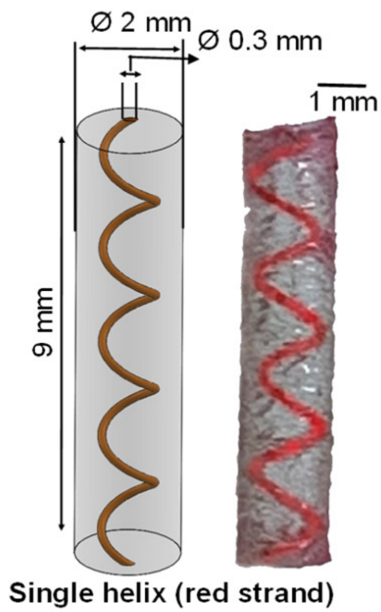

Figure 1.7: PDMS pillars with 3D microfluidic channels inside [40].

The first solution is to microchannel liquid metals to the elastomer [41]. Conductive liquids were introduced to provide the resistance needed in piezoresistive sensors. Low-melting-point metals and metal alloys, as well as ionic liquids, are examples of conductive liquids. Since it is liquid at room temperature and has lower toxicity than mercury, eutectic gallium–indium (EGaIn liquid metal) is commonly employed as a conductive fluid (Hg). However, other conductive fluids, ionic liquids, and ionic solutions, including aqueous sodium chloride, have been employed (NaCl). Ionic liquids and eutectic gallium–indium have also been combined in soft strain sensors and utilized independently in soft pressure sensors [42]. Although liquid metals have excellent conductivity, they cannot be used at temperatures below their melting point, and their density is often substantially higher than that of most elastomeric substrates. Ionic liquids have low density, are inexpensive but have low conductivity, and frequently experience considerable temperature drift due to the temperature-ion concentration correlation, as well as long-term instability due to electrolysis when subjected to electrical current [43].

Various nanomaterials have been investigated for use as conductive materials. Nanoparticles (NPs) with diameters ranging from 10 to 100 nm are being used in an emerging technique for robust real-world applications of flexible sensors. Several investigations have demonstrated the capacity to manipulate the kind of NPs, beginning with cores consisting of pure metals such as Au (gold), Ag (silver), Ni (nickel), Co (cobalt), Pt (platinum), Pd (palladium), Cu (copper), etc [44]. In recent years, however, distinctive two-dimensional (2D) layered materials such as graphene, carbon nanotubes, carbon black, MXene, metal oxides, metal-organic frameworks, and conductive polymers have been widely utilized in diverse piezoresistive sensor sectors. Compared to other conductive materials, carbon-based materials have excellent mechanical properties, low density, and simple storage and processing properties [45]. Yamada et al. fabricated carbon nanotubes on Polydimethylsiloxane (PDMS) substrate for wearable devices and successfully measured 280% changes in strain [46]. For a better sense of strain, multi-walled carbon nanotubes were introduced, which are able to work in higher strain ranges of 300% or more. The multi-walled carbon is also more durable and better suited for long-term costs [47]. With the enhancement of 3D printing of multi-walled carbon [48], studies were more focused on wearable designs and fabrications and not surgical aspects. Depending on their application, required sensitivity, cost, and mechanical properties, various types of particles were used over time, such as carbon ink [49, 50], silver nanowires[51], copper nanowires [52] and graphite [53].

Among various carbon-based materials, graphene has received increasing interest in piezoresistive sensors owing to its superior mechanical properties, easy manufacturing technique, and exceptional conductivity [54]. Several methods can be used to use graphene with Polydimethylsiloxane (PDMS). Graphene and Polydimethylsiloxane (PDMS) can be utilized in a number of ways. The most commented method involves uniformly dispersing graphene in ethanol using ultrasonic waves and then adding the PDMS primary agent to the graphene [55]. Laser-induced graphene (LIG) is another way to break the layer structure of graphene. The sharp rise in the localized temperature due to lattice vibrations by laser irradiation easily breaks the bond in graphene [56]. Although the aforementioned strategies all indicate promising results, they are costly, and most cannot undergo sterilization.

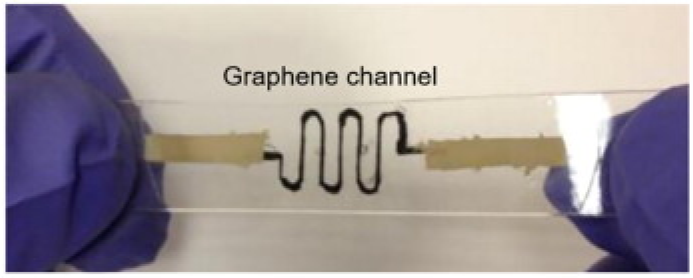

Figure 1.8: graphene channel embedded in soft body [57].

The two-dimensional transition metal carbides and nitrides known as MXenes, as well as graphene and its derivatives, are all extremely sensitive to changes in ambient conditions, including pressure. A matrix made of conducting polymers, however, can improve the performance of other conducting or semiconducting structures based on charge transfer. Consequently, a wide range of tactile sensors with specialized detecting qualities can be created thanks to the design of such CP-based hetero-composites [58]. In terms of their work range and sensitivity, Table. 1.1.4 compares several piezoresistive particles.

While using metal-impregnated emulsions for shape sensing is cheap, the proposed fabrication methods are often complicated and costly. For example, in the proposed fabrication processes, ultrasonication is necessary for the homogeneous dispersion of the metal particles and breakage of the agglomerations [59]. In recent years, the hydrogel has been included in strain sensors. Hydrogels, with their unique characteristics of swelling behavior, flexibility, high biocompatibility, and porosity, have proved their adaptability in numerous academic and industrial domains, including biomedical engineering, sensor, and actuator [60]. Due to its flexibility and conductivity, gelatin composite hydrogel can be employed as a mechanical sensor [61]. Later on, A multipurpose platform for a highly recoverable tactile sensor and stretchable strain sensor based on polyvinylidene fluoride (PVDF)-Ppy reinforced gelatin organohydrogel was reported [62]. Gelatin is a functional protein made by partially denaturing natural collagen. Due to their unique porous structure, high capacitance, flexibility, nontoxicity, superior biocompatibility, and biodegradability, gelatin conductive hydrogels are regarded as potential materials for constructing flexible wearable sensors. A flexible ionic gelatin-glycerol hydrogel was developed by Hardman et al.[63].for soft sensing applications, as shown in Fig 1. The resulting sensor system can withstand strains of up to 454%, is self-healing at room temperature, inexpensive and simple to manufacture, stable over extended periods of time, and biocompatible and biodegradable. Numerous reinforcing species (such as metal nanoparticles, carbon-based compounds, and polymers) have been added to gelatin over the past few decades, and the resultant gelatin conductive hydrogels exhibit amazing advances in various respects [64].

Figure 1.9: Self-healing ionic gelatin/glycerol hydrogel strain sensor [63]

As previously mentioned, Due to their superior electrical conductivity, carbon materials, such as carbon nanoparticles/nanowires/nanotubes, graphene, and graphene oxide, are ideal molecules for building 3D-conductive networks within polymer matrices. In numerous investigations, the combination of carbon compounds and gelatin yielded encouraging results [65, 66]. To obtain great deformability, Hsiao et al. synthesized multi-walled carbon nanotubes (MWNTs) in a gelatin solution [67]. Attention must be drawn that stretchable electronics based on hydrogels encounter significant difficulty with dehydration. To prevent water molecules from evaporating and maintain the structure of a hydrogel, techniques such as encapsulation by an elastic substrate and solvent replacement are employed [68].

1.1.5 Graphene-based sensors

Due to their exceptional electrical conductivities and distinctive nanoscale flexibility, graphene-based piezoresistive sensors are particularly appealing [79]. Highly flexible and sensitive sensors

Table 1.1: Comparison of flexible piezoresistor-based tactile sensor.

Author	Functional Material	Working range	Sensitivity
Ahmed et al. [69]	Nichrome	0.266 to 2.248 N	1.25 V/N
Ma et al. [70]	MXene	-	gauge Factor $\sim$ 180.1
Xu et al. [71]	3D graphene	66 kPa	gauge Factor $\sim$ 584.2
Liu et al. [72]	Graphene	90% of strain	-
Boland et al. [73]	Graphene	-	gauge factors $\geq$ 500
Jia et al. [74]	Graphene oxide	100–200 Pa	178.1 kPa–1
Zhao et al. [75]	Multiwalled*	$\leq$ 140 Pa	83.9 kPa–1
Lim et al. [76]	Hydrogel and silver nanowires	20% of strain	-
Zhang et al. [77]	Copper	0–7 N	206.6 mV/N
Tata et al. [78]	Carbon	0%–50% of starin	24.15 mV/ϵ (%)

*: Carbon nano-tube

have been created using graphene-based microstructures since graphene has been assembled in various forms of two-dimensional (2D) or three-dimensional (3D) macroscopic, freestanding constructions using a few distinct processes [80]. By introducing flexible polymer into 3D graphene frameworks or uniformly dispersing graphene sheets within flexible polymer matrices, graphene/flexible matrix composites were created [81]. Due to their greater flexibility, flexible polymers like polydimethylsiloxane (PDMS), Ecoflex, polyimide (PI), and polyurethane (PU) are frequently employed as substrates or matrices [82]. Moreover, Due to their distinctive structural interconnectivity, high porosity, and stable mechanical properties, 3D graphene architectures, such as foams, hydrogels, aerogels, and sponges, were simple to infiltrate with liquid polymers [83, 84]. Incorporating hydrogen and graphite produces self-healing properties. For flexible devices that may be included into fully functional applications, intrinsic self-healing based on molecular interactions with quick and reversible healing capabilities, such as hydrogen bonding, is preferable to extrinsic self-healing for strain sensors [85].

The functionality of sensors used in portable electronic devices should not be confined to a single stimulus operating alone, such as strain, twist, or pressure [87]. Widespread applications in multiple-degrees-of-freedom environments require multidimensional sensors capable of sensing complicated multiaxial strains. Creating conductive networks with an anisotropic structure is one

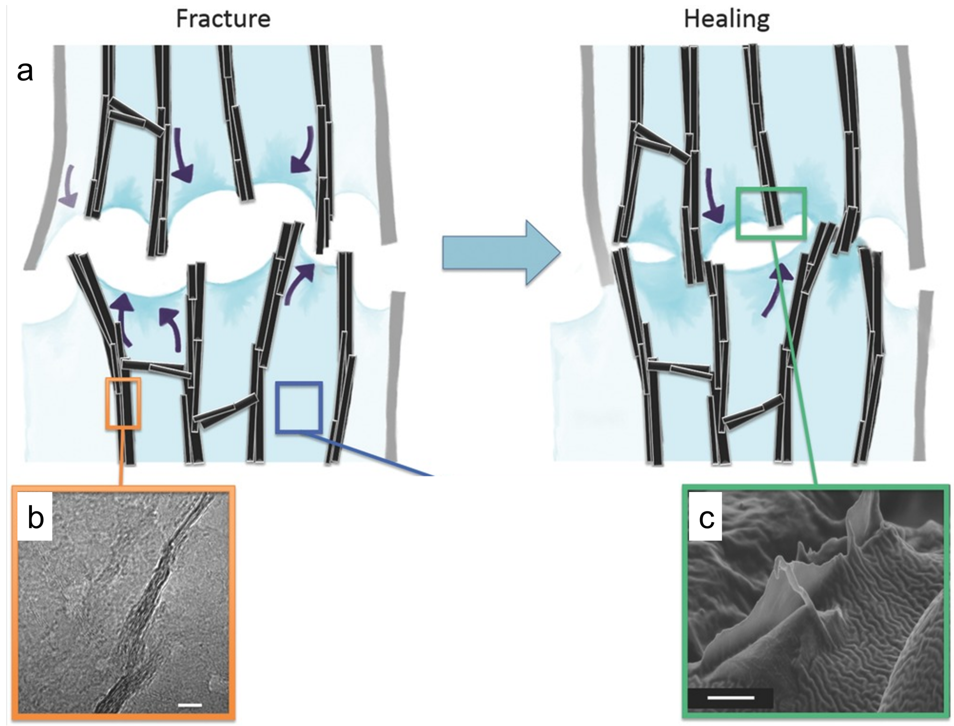

Figure 1.10: a) A diagram of the healing procedure. b) The network walls consist of intertwined graphene flakes (transmission electron micrograph). d) Fracture exposes the carbon network walls (scanning electron micrograph of a fracture surface). Capillary forces caused by polymer flow bring the wall together, re-establishing the link between the network's walls, while the polymer's reversible bonds allow for complete matrix repair [86].

method for designing multidimensional sensors capable of sensing multiaxial strains [88].

1.2 Motivations

The creation of smart tactile sensing systems remains a subject with numerous technical and scientific obstacles. Strong interdisciplinary efforts are required not just for better tactile sensors but also for adequate algorithms to deal with the collected data. Advances in materials, fabrication processes, and signal processing can all help to improve smart tactile sensing [24].

Sonification is required to break the link between particles and conductive polymers when incorporating particles such as graphite into conductive polymers [90]. It is safe to assume that this method is costly and complicated. Sonification should be eliminated to simplify and reduce the cost of the procedure.

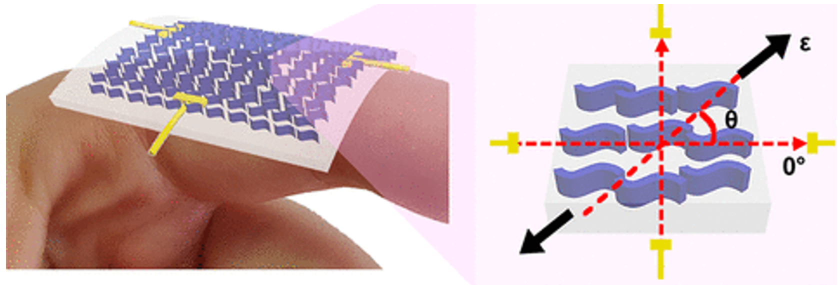

Figure 1.11: Stretchable strain vector sensor capable of concurrently detecting strain directions and amplitudes [89].

Sterilization was another major consideration during the sensor-making process [10]. Due to their wire system, it is not possible for piezoresistive sensors to undergo sterilization; thus, the material and manufacturing method must be inexpensive and simple so that the sensor is suited for single use only.

1.3 Research objectives

To address the identified knowledge gaps outlined in Section 1.2, the specific aims of this study were:

(1) To propose and validate a soft sensing principle for moldable elastomeric-based sensing,

(2) To identify an elastomeric composite and its associated fabrication process for molding and encapsulation of the proposed composite into soft flexures,

(3) To develop an accurate calibration schema for the proposed soft sensors, and

(4) To prove the concept of the proposed embedded force-torque sensing for intraluminal minimally invasive procedures.

1.4 Thesis layout

This thesis is prepared in manuscript-based style according to the ”Thesis Preparation and Thesis Examination Regulations (version-2022) for Manuscript-based Thesis” of the School of Graduate Studies of Concordia University. This dissertation includes five chapters with the following contents:

Chapter 1 presents the results of a critical literature review of force and shape sensors for soft robots with regard to the state-of-the-art modeling approaches, methods, and knowledge gaps.

Chapter 2 describes the design, prototyping, and validation of the proposed one-degree-of-freedom (1-DoF) soft force sensor. This chapter is based on the author's following publication:

(1) Tannaz Torkaman, Majid Roshanfar, Javad Dargahi, Amir Hooshiar, "Analytical Modeling and Experimental Validation of a Gelatin-based Shape Sensor for Soft Robots." 2022 International Symposium on Medical Robotics (ISMR). IEEE, 2022 [91]

The contribution of the second author was in preparation for the experimental setup and manuscript drafting. The third and fourth authors' contributions were in supervision, funding, and academic advice.

Chapter 3 reports the second proposed sensor of this thesis which was a 3-DoF force sensor. The contents of the chapter are partially based on the author's following contribution:

(1) Tannaz Torkaman, Majid Roshanfar, Javad Dargahi, Amir Hooshiar, "Accurate Embedded Force Sensor for Soft Robots with Rate-dependent Deep Neural Calibration." 2022 IEEE Conference on Robotics and Sensor Environments (ROSE). IEEE, 2022 (Accepted)

The contribution of the second author was in preparation for the experimental setup and manuscript drafting. The third and fourth authors' contributions were in supervision, funding, and academic advice.

Chapter 4 presents the third proposed sensor of this research which was a 6-DoF force-torque sensor for intraluminal procedures. The contents of this chapter were based on the author's following under-review contribution:

(1) Tannaz Torkaman, Majid Roshanfar, Javad Dargahi, Amir Hooshiar, "Embedded Six-DoF Force-Torque Sensor for Soft Robots with Learning-based Calibration." IEEE Sensors Journal (under review)

The contribution of the second author was in the preparation of the experimental setup and manuscript drafting. The third and fourth authors' contributions were in supervision, funding, and academic advice.

1.5 Contributions

This study was, to the best of the author's knowledge, the first to address the limits of manufacturing and the complexity of present methods for producing piezoresistive sensors. Experimental validation of the suggested sensing principle with nonlinear calibration was shown to be of enough accuracy for intraluminal procedures, and the proposed mechano-electrical model of the sensing principle and its validation were performed that allow future researchers to look into design optimization.

The results of this research have been published as two conference papers and are under review as a journal paper:

(1) Tannaz Torkaman, Majid Roshanfar, Javad Dargahi, Amir Hooshiar, "Analytical Modeling and Experimental Validation of a Gelatin-based Shape Sensor for Soft Robots." 2022 International Symposium on Medical Robotics (ISMR). IEEE, 2022

(2) Tannaz Torkaman, Majid Roshanfar, Javad Dargahi, Amir Hooshiar, "Accurate Embedded Force Sensor for Soft Robots with Rate-dependent Deep Neural Calibration." 2022 IEEE Conference on Robotics and Sensor Environments (ROSE). IEEE, 2022 (Accepted)

(3) Tannaz Torkaman, Majid Roshanfar, Javad Dargahi, Amir Hooshiar, "Embedded Six-DoF Force-Torque Sensor for Soft Robots with Learning-based Calibration." IEEE Sensors Journal (under review)

Chapter 2

Analytical Modeling and Experimental Validation of a Gelatin-based Shape Sensor for Soft Robots

Shape sensing of soft robots has been a challenge due to the large deformation of the soft robots and their low stiffness. In this study, a simple yet accurate soft sensor for soft robotic applications with small force ranges was proposed, modeled, prototyped, and experimentally validated. The proposed soft sensor is based on a gelatin-graphite composite that exhibited piezoresistive properties. The sensing element was molded to a cylindrical shape and was embedded in a soft flexural structure as a common type of soft flexural robots. Afterward, a mechano-electrical model for predicting the changes in the resistance of the sensing element was proposed, and its predictions were validated through an experimental study. To demonstrate usability for force sensing, the sensor was calibrated with a nonlinear model and exhibited a force measurement range of 0.035-0.82 N with an average absolute error of 3.7% and a resolution of 4%. Also, the mechano-electrical model was fairly accurate in predicting the piezoresistivity phenomenon of the sensing element under large bending deformations.

2.1 Related Studies

Changes in the dimensions of a piezoresistive sensor due to applied force or pressure will result in changes in its resistivity, which is the working principle of this type of sensor [30]. Several strategies have been proposed to integrate the Piezoresistive sensor with MIS [31]. Bandari et al. [32] gathered the improvements for this approach from the early studies in the area of intravascular neurosurgery when piezoresistive strain gauges were used on silicon. The silicon base enables better deformation while the resistance in the gauges changes [33]. Later on, gauge strain sensors with the same principle were used to provide haptic feedback for laparoscopy equipment such as grasper. High precision and the safety of the body that is made of silicon rubber are the two significant advantages of this method [34, 35].

The variety of application and fabrication methods paved the way for researchers to introduce more creative designs, whether the goal is to implement the sensor onto a da Vinci robotic system [36] or a catheter-based cardiac surgery [37]. One of the features of a piezoresistive sensor that plays an essential role in robotic surgery is its ability to exhibit an acceptable stretch [38]. While elastomers were previously introduced to soft robots, using a conductive material embedded with the elastomer is the key to creating piezoresistivity for sensing ability [39]. The first solution is to microchannel liquid metals to the elastomer [41]. The primary liquid metal used for this method is eutectic gallium-indium (EGaIn) [92]; while it meets the conductivity requirement, the higher cost compared to other methods and the complicated fabrication are considered to be the limitations of this method [41]. Therefore in some other studies, saltwater is used as the conductive liquid. While using NaCl is desirable because of the nontoxicity, in addition to the lower cost [93], its conductivity compared to other materials is not relatively high [41]. That is why metals were introduced to tackle the issue. Using carbon-based fillers and nanoparticles enables the sensor to present higher resistivity variation. When these metal particles combine with silicon polymers, they show better flexibility and cost-efficiency [94]. Yamada et al. fabricated carbon nanotubes on Polydimethylsiloxane (PDMS) substrate for wearable devices and successfully measured 280% changes in strain [46]. For a better sense of strain, multi-walled carbon nanotubes were introduced, which are able to work in higher strain ranges of 300% or more. The multi-walled carbon is also more durable and better suited for long-term costs [47]. With the enhancement of 3D printing of multi-walled carbon [48], studies were more focused on wearable designs and fabrications and not surgical aspect. Depending on their application, required sensitivity, cost, and mechanical properties, various types of particles were used over time, such as carbon ink [49, 50], silver nanowires[51], copper nanowires [52] and graphite [53].

While using metal-impregnated emulsions for shape sensing is cheap, the proposed fabrication methods are often complicated and costly. For example, in the proposed fabrication processes, ultrasonication is necessary for the homogeneous dispersion of the metal particles and breakage of the agglomerations [59]. Recently, hydrogel-based biosensors have been introduced for biosensing applications such as wound healing monitoring and motion sensing [95]. Such sensors consist of a hydrogel matrix filled with an aqueous electrolyte. While the elastic properties of the matrix make the hydrogel deformable, the electrolytic properties of the filler make it conductive. The choice of the filler containing the hydrogel may exhibit piezoresistive [96] or piezoelectric [97] properties. In addition, hydrogels exhibit unique properties such as full recovery after large deformations and self-healing [98]. Moreover, Water-soluble additives such as tannic acid, sodium chloride, and zinc sulfate can be mixed with hydrogel to provide more resistance change [98].

Among different hydrogels, Gelatin is the most extensively adopted for biomedical applications because of its excellent biocompatibility and biodegradability [99]. In this study, the authors have designed, fabricated, and tested a novel gelatin-based shape sensor for flexural soft robots. In the following, the performance requirements, design of the sensor and the representative soft robot, and multi-physics modeling of the gelatin-based sensing element, along with the fabrication process and experimental studies, are provided.

Among different performance criteria, sensing range, resolution, root-mean-square error (RMSE), and hysteresis have been emphasized for shape sensing in soft robots [100, 32]. For minimally invasive surgery applications, the shape sensors are typically required to exhibit a measurement range of 0 to 2 N, a resolution of 5% of the full-scale, i.e., 0.1 N, RMSE of less than 5% of full-scale, i.e., RMSE$\leq$ 0.1N, and hysteresis of less than 5%. Typically for the estimation of hysteresis, a cyclic loading on the sensor is performed, and the hysteresis is estimated using [101]:

$$H = \frac{\int_{t=0}^{T} f(t)dv}{\int_{t=0}^{\frac{T}{2}} f(t)dv} \times 100, \tag{1}$$

where H is the hysteresis as a percentage, $t = 0$ and T indicate the beginning and the ending times of a given full cyclic loading, f is the mechanical stimulus applied on the sensor, e.g., force, and v is the sensor's output, e.g., voltage.

2.2 Contributions

The main contributions of this study were: 1) the addition of graphite micro-platelets to the gelatin for inducing piezoresistivity, 2) proposing a new sensing principle for large deformation of flexural soft robots, 3) mechano-electrical modeling of the sensing principle and its validation, and 4) experimental validation of the proposed sensing principle with nonlinear calibration.

2.3 Materials and Methods

2.3.1 Sensing Principle and Design

The sensing principle of the proposed sensor in this study is based on finding a nonlinear correlation between the deformation-induced changes in the electrical resistance of a soft sensor. To be applicable in soft robotics applications, the sensor's stiffness shall be comparably less than the robot's stiffness to avoid deformability reduction caused by adding the sensor. Given that soft flexural robots are typically made of soft elastomers, especially for surgical applications, the sensor's stiffness shall be significantly small [31]. Therefore, in this study, the authors have proposed a very soft gelatin-based shape sensor for flexural robots and demonstrated its performance in a representative example.

To this end, a single-chamber soft flexure (soft body) was designed and reinforced with a linear coil spring. Fig. 2.1 depicts the schematic geometrical design of the flexure. This type of flexural

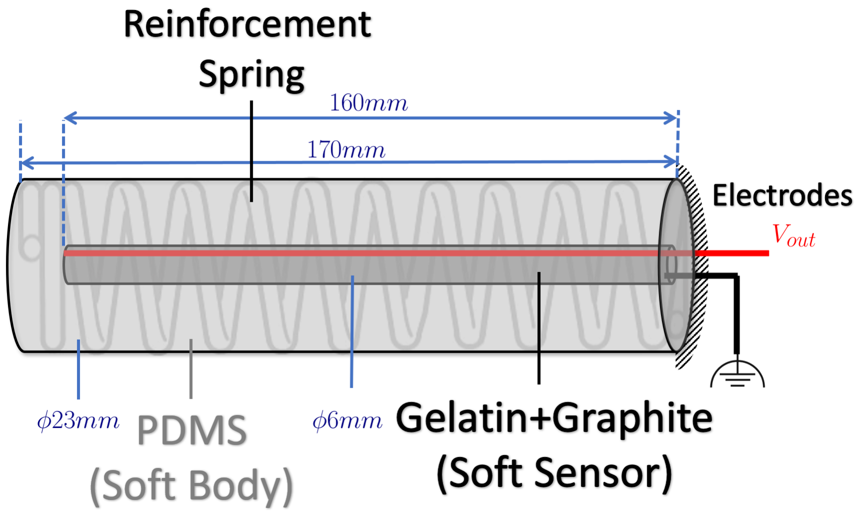

Figure 2.1: The structural design of the sensor with gelatin/graphite capsulated inside PDMS.

body is amongst the simplest structures for soft robots and has frequently been adopted for medical applications, e.g., [102]. The flexural body had a central blind cylindrical chamber that served as a mold and was filled with the proposed gelatin-based sensing element. Also, two copper wires were placed at the bottom and top of the center during the molding that was used in a voltage divider to measure the changes in the voltage between them. This design allowed for encapsulation of the sensing element within the flexure would eliminate the concerns about the acute biocompatibility of graphite used in the sensing element.

2.3.2 Fabrication

Fig. 2.2 shows the fabrication process for the soft body and soft sensor. To prepare the soft body, a cylindrical mold as fabricated using a 3D printer (Replicator+, MakerBot, NY, USA) with poly-lactide acid (PLA) filaments. Polydimethylsiloxane (PDMS) was prepared by mixing the PDMS base (Sylgard 184, Dow Corning, MI, USA) with its curing agent in a 10:1 ratio [103]. The mixture was stirred for 5 minutes to achieve homogeneity. The mixture was degassed by exposing it to 30 in-Hg vacuum pressure for 10 minutes. The mixture was afterward injected into a 3D-printed mold while the coil spring was placed inside the mold. The mold was then rested for 24 hours at $25°C$ for the final setting.

The soft sensing element was prepared by impregnating gelatin with graphite microplatelets (Graphinox, India). As shown in Fig. 2.2, the gelatin sachets were soaked in $10°C$ water for 2 minutes. The soaked sachet was then transferred to 50 mL boiling water and stirred until completely dissolved. Afterward, 5mL graphite micro-platelets were added to the solution, and the emulsion was stirred to cool down to room temperature. The emulsion was afterward injected into the soft body's chamber using a 10mL injection syringe, while two copper wires were previously placed and secured into the soft body's chamber. The soft body was afterward kept at $4°C$ for 2 hours until the gelatin was set. After setting, the injection site on the chamber has sealed another layer of PDMS was encapsulated in the soft sensor. The total encapsulation of the gelatin-based sensor after setting at $4°C$ was also crucial to avoid gelatin melting at room temperature as its confinement with PDMS does not allow volumetric changes in gelatin necessary for melting.

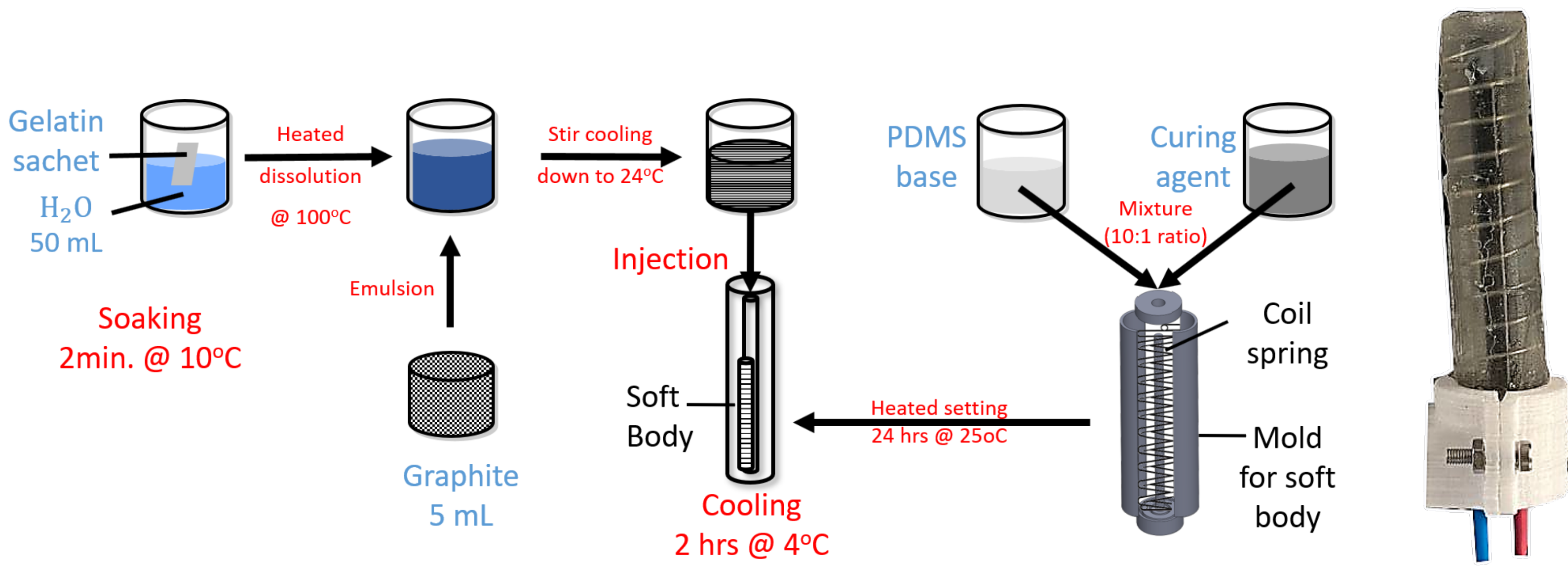

(a) (b)

Figure 2.2: Fabrication of gelatin and graphite mixture inside PDMS layer.

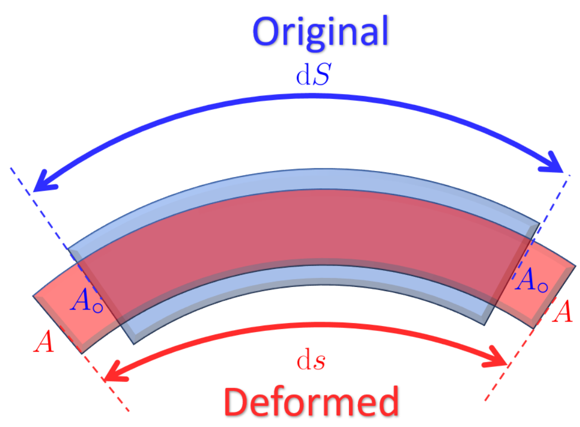

Figure 2.3: Differential element of the sensing element under deformation.

2.3.3 Modeling and Mechano-electrical Simulation

The gelatin-graphite composites exhibit piezoresistivity; thus, their electrical resistance changes while undergoing deformation. This phenomenon may be related to the deformation-induced changes in the effective diameter and length of the sensing element inside the soft body. In the flexural soft robots, the main deformation mode is bending, and the measurements of interest in soft robotic applications are bending angle [31] and lateral tip forces [104, 105]. Therefore, the objective of the modeling was to find the relationship between the electrical resistance of the sensing element and the bending angle. Since the bending angle and lateral tip force are directly related, in this study, the shape sensor was used to measure the lateral tip force as a surrogate for the bending angle.
The resistance of the sensing element R was modeled as a function of specific resistivity ρ, cross-sectional area A, and length L. Before the deformation, the specific resistivity ρ of the sensing element was obtained using its initial resistance $R_\circ$:

$$R_\circ = \rho \frac{L_\circ}{A_\circ}, \tag{2}$$

Bending deformation would change both L and A as it induces longitudinal strain along the sensing element. Since the sensing element was assumed incompressible because of its high water content and elastomeric nature, the crossectional area of the sensing element would inevitably reduce to compensate for its longitudinal elongation. Thus, during the deformation, the resistance of the sensing element would be:

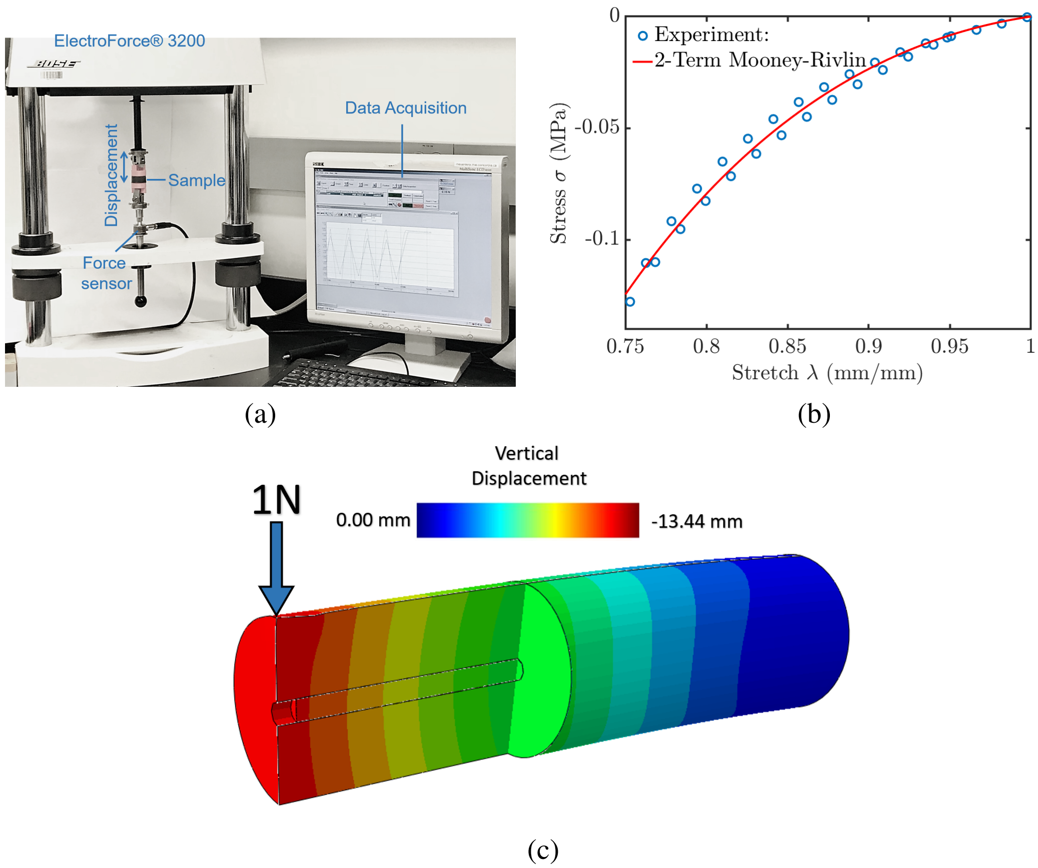

Figure 2.4: (a) Setup and a representative sample under compression test, (b) a stress-stretch diagram for the PDMS sample, and (c) deformation of the finite element model.

$$R = \rho \frac{L}{A}, \tag{3}$$

Fig. 2.3 compares the deformed and original shapes of an infinitesimally small element of the sensing element. Assuming dS as the original length of the differential element and ds as its deformed length, the incompressibility constraint necessitated:

$$Ads = A_{\circ}dS \Rightarrow A = A_{\circ}\frac{dS}{ds} \tag{4}$$

On the other hand, based on continuum mechanics, longitudinal stretch λ for a 1D differential element under bending-induced elongation is:

$$\lambda = \frac{ds}{dS} = \frac{L}{L_\circ}, \tag{5}$$

Thus, Eq. 4 was simplified to:

$$A = A_\circ \lambda^{-1} \tag{6}$$

Therefore, for a given deformed length L, the mechano-electrical model would predict an electrical resistance of:

$$R = \rho \int_0^L \frac{ds}{A}. \tag{7}$$

Changing the Eulerian coordinates (deformed) to Lagrangian coordinates (original), the integral simplified to:

$$R = \rho \frac{1}{A_\circ} \lambda^2 \int_0^{L_\circ} dS = R_\circ \lambda^2 \tag{8}$$

Therefore, the sensing element would exhibit quadratic resistance change with the nonlinear stretch caused by large bending. To simulate this phenomenon, the change in length of the sensing element was simulated using the finite element method for a representative loading condition, and the computational stretch was used to predict the change in the sensing element's resistance. To this end, the geometrical model of the sensor (Fig 2.1) was imported in Abaqus (R2021, Dassault Systemes, France) and was meshed with tetrahedral meshes. Hyper-elastic material models were used for both the soft body and sensing element. The mesh size was selected based on a mesh-independency test on the total strain energy of the model. Also, Dirichlet and Neumann boundary conditions were applied to the base of the soft body and sensing element. The tip of the soft body was subjected to a downward 1N concentrated force. The material properties of the FEM solution can be seen in Table. 2.1. The average elemental stretch of the numerical solution was obtained and utilized to predict R. Also, $R_\circ \approx 329\Omega$ was experimentally obtained using a multimeter on the prototyped sensor.

2.3.4 Material Characterization

In order to obtain the mechanical properties of PDMS rubber and the sensing element, three standard samples of each were prepared. The samples were cylinders of $D_\circ = 29$mm diameter and $H_\circ = 12.5$mm height (Fig. 2.4(a)). The samples were molded in 3D-printed molds, were prepared following the fabrication process explained in Sec. 2.3.2, and were tested as per ISO 7743:2017 [106] using a universal testing machine (Electroforce 2000, TA Electronics, DE, USA) (Fig. 2.4(a). Each sample underwent four triangular compression cycles with a displacement rate of 10 mm/min and a range of 0.625mm to 3.125mm, which corresponds to 5% to 25% compressive strains, respectively. The first three cycles were considered as conditioning cycles; thus, the force and displacement data of the fourth compression cycle was used for analysis. The stretch-stress curves of the samples were obtained from the force (f) and displacement (x) data and were fitted with a two-term Mooney-Rivlin model (Eq. 9) [101]:

$$\sigma = 2(C_{10} + \frac{C_{01}}{\lambda})(\lambda^2 - \frac{1}{\lambda}), \tag{9}$$

where, $\sigma = \frac{4f}{\pi D_\circ^2}$ was nominal stress in MPa, $\lambda = 1 + \frac{x}{H_\circ}$ was the compressive stretch, and C_{01} and C_{10} were the material properties. The fittings were performed using the Curve-fitting Toolbox of Matlab 2021b (Mathworks, MA, USA). Fig. 2.4(b) shows a representative stress-stretch diagram of a PDMS sample with the fitted 2MR model. The average goodness-of-fit among all the samples was 0.9882 with a root-mean-square error (RMSE) of 0.004 MPa.

Although hyperelastic material model was used in this study, the author acknowledges the PDMS soft body and the gelatin-graphite composite are hyperviscoelastic in nature. The hyperelastic assumption here may lead to non-negligible error between theoretical prediction and experimental findings. Nevertheless, the author has shown that with a rate-dependent neural calibration the rate-dependency properties of the soft body can be adequately addressed. The main use of the proposed simplified theoretical model was merely to show the phenomenological relationship between the sensing element's output voltage and external mechanical forces acting on the soft body.

Fig. 2.4(c) shows the displacement distribution on the soft body and sensing element. The maximum vertical displacement of the tip of the deformed soft body was -13.44mm. This vertical

Table 2.1: Material properties of the model components.

Material	Hyperelastic model	Coefficients
PDMS	Two-termvMooney-Rivlin	C_{01}=-0.3266 MPa C_{10}=0.3207 MPa
Sensing element	Two-term Mooney-Rivlin	$C_{01} = -5.9074 \times 10^{-5}$ MPa $C_{10} = 5.6102 \times 10^{-5}$ MPa

deformation resulted in a longitudinal stretch of $\lambda = 1.01543$ that corresponded to a relative change in the resistance of $(R - R_\circ)/R_\circ \times 100 \approx 3.11\%$.

2.4 Experimental Validation

To preliminarily validate the mechano-electrical model, an experiment on the prototyped sensor was performed.

2.4.1 Test Protocol and Setup

The soft sensor was installed on a 3D-printed housing platform. The platform was then mounted on an ATI mini40 force/torque sensor (ATI Industrial Automation, NC, USA). Fig. 2.5 shows the experimental setup for this study. The ATI sensor was used to measure the applied force on the sensor applied by a desktop CNC device. Meanwhile, an Arduino Uno was used to measure the voltage changes in the sensor. The sensor was serialized with a 300Ω resistor to form a voltage divider circuit together bridged to +5v excitation. The CNC device was programmed to apply a 15mm sinusoidal vertical displacement with a frequency of 1Hz at the tip of the soft body. Then displacement cycles were performed.

2.4.2 Results

The temporal changes in the resistance of the sensor captured during the experiment and the theoretical prediction are shown in Fig. 2.6. The results show a fair agreement between the theoretical prediction and experimental results. The maximum error between the theory and experiment was 3.18Ω at the end of the fifth cycle, which corresponded to a relative error of approximately 1% of the initial resistance $R_\circ = 329\Omega$. In spite of the large deformation of the soft body and sensor, the

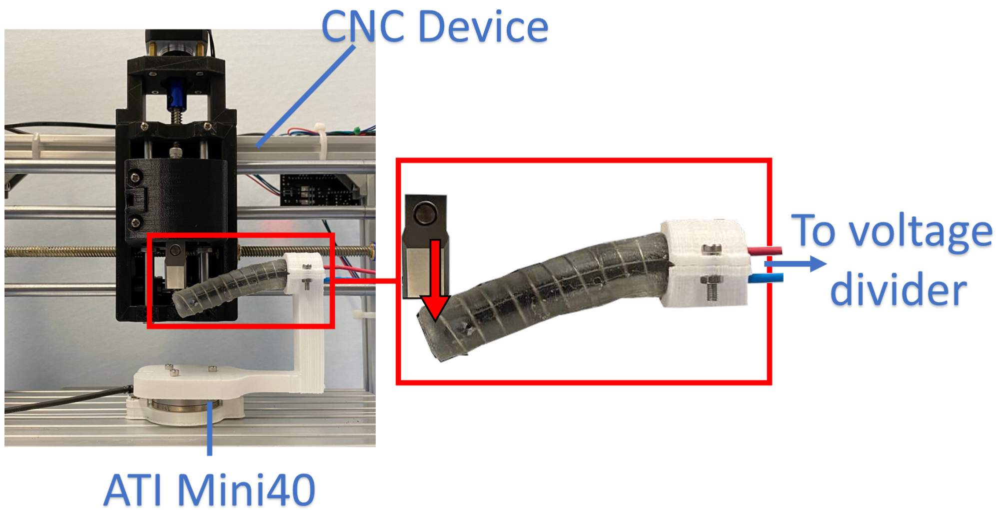

Figure 2.5: Test setup for experimental validation.

model was fairly accurate in capturing the effect of geometrical changes on the sensor resistance. The authors believe capturing the effects of geometrical nonlinearity (large deformation) through λ into the model has contributed to the model's accuracy.

Fig. 2.6(b) shows the variation of the sensor voltage V with the tip lateral force F. This figure shows two plateaus for forces approximately less than 0.035N and more than 0.820N that show the lower and upper bound of the range of the sensor. The lower band is mainly affected by the sensitivity of the sensing element to low forces, and the upper bound mainly happens due to the saturation of the sensing element, beyond which the sensor cannot measure the force. By changing the geometry of the design, the model is capable of capturing the required force range. However, the implemented force in the setup is within the acceptable range for the ablation procedure. To demonstrate the usability of the proposed sensing principle, the F–V_{OUT} relationship of the sensor was fitted with a nonlinear model that could smoothly capture both lower and upper bounds. Eq. 10 shows the proposed calibration model. Matlab curve fitting toolbox was used to determine the calibration coefficients summarized in Table 2.2. While saturation of the sensing element could not be captured with the proposed model, the initial plateau for low forces could be captured as the low forces cause a negligible longitudinal stretch in the sensing element, but it drastically increases when bending is beyond small deformation ($\approx 5°$ angle). Considering a full-scale force range of 0–0.94N in this

Table 2.2: Calibration coefficients of the sensor and goodness-of-fit (R^2)

Fitting Parameters				Goodness-of-fit
a	b	c	d	R^2
0.2308	0.02445	22.68	121.6	98%

experiment and with the average error between the calibration function and the ground truth force measured at 0.038 N, the relative average error to full-scale was 4%. Moreover, the resolution of the force sensor was 0.035, which corresponded to 3.7% of the full-scale. Also, the evaluation of Eq. 1 on the temporal variation of the experimental and calibration data showed that the hysteresis of the calibration model was zero, while the experimental data exhibited a hysteresis of 7.4%. Thus, the calibration model was unable to compensate for the intrinsic hysteresis of the sensor. The sensor's intrinsic hysteresis is related to its viscoelastic nature and its high water content.

$$F = \frac{a}{(b + c \cdot e^{-d \cdot V_{OUT}})} \tag{10}$$

2.5 Summary

In this paper, the combination of gelatin and graphite was used as a piezoresistive sensor capsulated inside PDMS to form a soft sensor. The proposed sensor was modeled, and the model was validated experimentally. Also, the force-voltage characteristic diagram of the sensor was calibrated with a highly nonlinear model. The performance of the calibrated sensor showed its compatibility with the range and resolution requirements for soft robotic applications in the surgical field however, the proposed calibration model could not capture the intrinsic hysteresis of the sensor. For future work, the hysteresis property will be added to the proposed model and validated against the experimental result. The demonstrated usability of the proposed sensor and the proposed method will allow the researchers to optimize the shape of the sensor to maximize the shape sensor's sensitivity to deformation through simulation-based geometrical optimization of the shape, length, location, and cross-sectional area of the sensing element. Also, the simplicity of fabrication of the proposed

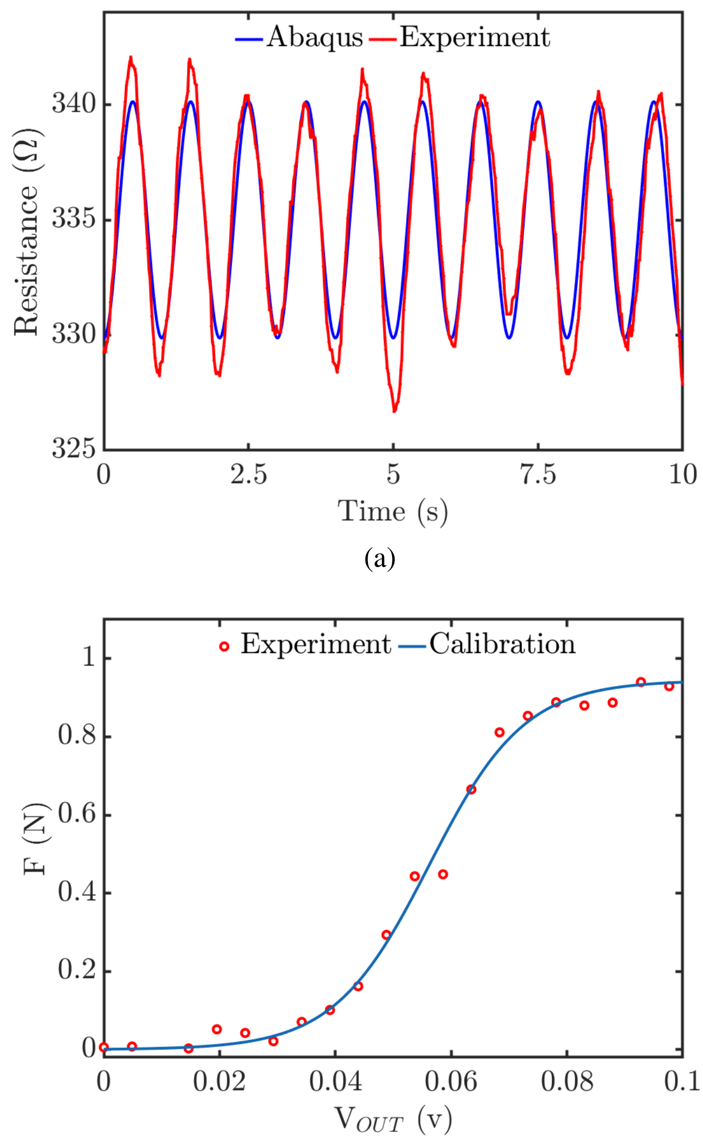

(a)

(b)

Figure 2.6: (a) Comparison of the experimental and theoretical changes in the resistance of the sensor, and (b) calibration curve of the sensor for force range from 0.035N to 0.82N.

sensor facilitates its application, especially as a disposable medical device. In future studies, a voltage-rate-dependent calibration model could be investigated to capture the sensor's intrinsic hysteresis. Also, multiple sensing elements at different locations of flexure can be studied to measure the 3D deformation of flexures. Moreover, optimized geometrical routing of the sensing element may facilitate 3D deformation measurements with a single sensing element.

Chapter 3

Accurate Embedded Force Sensor for Soft Robots with Rate-dependent Deep Neural Calibration

Embedding force sensors on soft robots have been a major challenge impeding accurate feedback control of soft robots. A major challenge in embedding force sensors onto soft robots is their rigidity, size, and shape. In this study, a soft smart polymer-based soft sensor for soft robotic application is proposed, prototyped, calibrated, and tested for force prediction accuracy. The sensing element of the proposed sensor was made of gelatin-graphite composite that we previously showed its piezoresistivity. Three sensing elements were molded into a soft body (soft robot), and variation of the voltage across them was measured in real-time in response to the external load. A rate-dependent deep neural calibration network was trained with the three voltages and their temporal rates when the soft body was subjected to tri-axial external forces in the range of ± 0.3 N. Afterwards; the calibrated sensor was used in a series of validation tests to assess its accuracy. The proposed calibration showed the goodness of fit of R^2 =0.98 with the mean-absolute error of 0.005 N. Also, the sensor exhibited mean-absolute errors of 0.007 ± 0.005 N, 0.008 ± 0.006 N, and 0.011 ± 0.008 N for estimating the external forces along the x, y, and z directions. Moreover, the proposed calibration did not exhibit observable hysteresis thanks to its rate-dependent calibration schema.

3.1 Related Studies

Fig. 3.1 depicts a schematic and representative use case of soft robots for intraluminal applications. Resistance in sensors was introduced using several approaches. Conductive liquids were introduced to provide the resistance needed in piezoresistive sensors. Low-melting-point metals and metal alloys, as well as ionic liquids, are examples of conductive liquids. Since it is liquid at room temperature and has lower toxicity than mercury, eutectic gallium–indium (EGaIn liquid metal) is commonly employed as a conductive fluid (Hg). However, other conductive fluids, ionic liquids, and ionic solutions, including aqueous sodium chloride, have been employed (NaCl). Ionic liquids and eutectic gallium–indium have also been combined in soft strain sensors and utilized independently in soft pressure sensors [42]. Although liquid metals have excellent conductivity, they cannot be used at temperatures below their melting point, and their density is often substantially higher than that of most elastomeric substrates. Ionic liquids have low density, are inexpensive but have low conductivity, and frequently experience considerable temperature drift due to the temperature-ion concentration correlation, as well as long-term instability due to electrolysis when subjected to electrical current [107]. In recent years, distinctive two-dimensional (2D) layered materials such as graphene, carbon nanotubes, carbon black, MXene, metal oxides, metal-organic frameworks, and conductive polymers have been widely utilized in diverse piezoresistive sensor sectors. Compared to other conductive materials, carbon-based materials have excellent mechanical properties, low density, and simple storage and processing properties [45]. Among various carbon-based materials, graphene has received increasing interest in piezoresistive sensors owing to its superior mechanical properties, easy manufacturing technique, and exceptional conductivity [54]. Several methods can be used to use graphene with Polydimethylsiloxane (PDMS). Graphene and Polydimethylsiloxane (PDMS) can be utilized in a number of ways. The most commented method involves uniformly dispersing graphene in ethanol using ultrasonic waves and then adding the PDMS primary agent to the graphene [55]. Although the aforementioned strategies all indicate promising results, they are costly, and most cannot undergo sterilization.

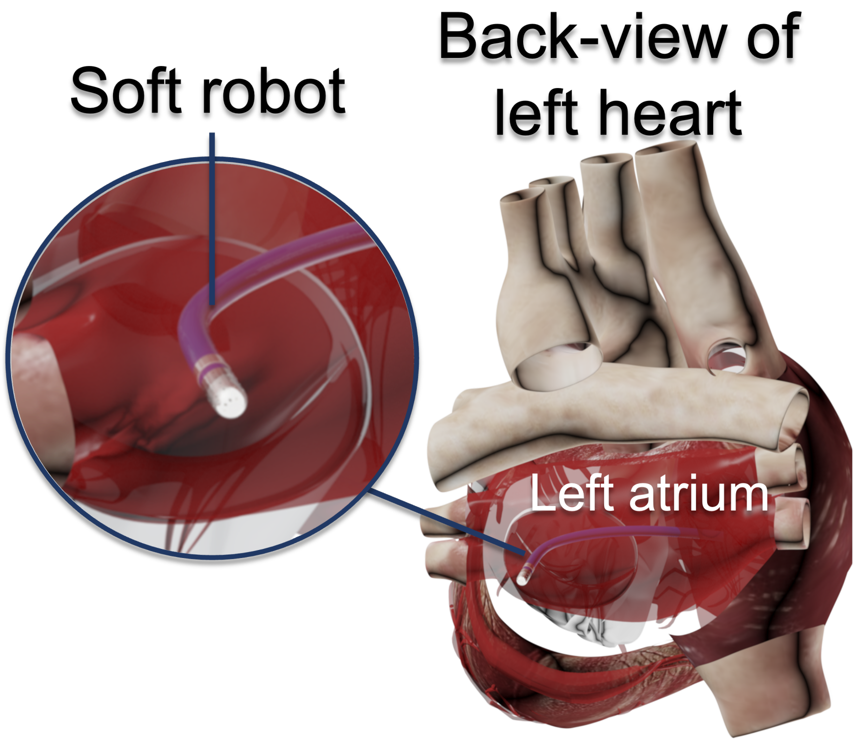

Figure 3.1: Schematic view of a soft robot in a force-sensitive surgical procedure, i.e., cardiac intervention.

In recent years, the hydrogel has been included in strain sensors. Hydrogels' unique characteristics of swelling, flexibility, high biocompatibility, and porosity have proved their adaptability in numerous academic and industrial domains, including biomedical engineering, sensor, and actuator [60]. Due to its flexibility and conductivity, gelatin composite hydrogel can be employed as a mechanical sensor [61]. Gelatin is a functional protein made by partially denaturing natural collagen. Due to their unique porous structure, high capacitance, flexibility, nontoxicity, superior biocompatibility, and biodegradability, gelatin conductive hydrogels are regarded as potential materials for constructing flexible wearable sensors. Numerous reinforcing species (such as metal nanoparticles, carbon-based compounds, and polymers) have been added to gelatin over the past few decades, and the resultant gelatin conductive hydrogels exhibit amazing advances in various respects [64].

As previously mentioned, Due to their superior electrical conductivity, carbon materials, such as carbon nanoparticles/nanowires/nanotubes, graphene, and graphene oxide, are ideal molecules for building 3D-conductive networks within polymer matrices. In numerous investigations, combining carbon compounds and gelatin yielded encouraging results [65, 66]. Attention must be drawn that stretchable electronics based on hydrogels encounter significant difficulty with dehydration. To prevent water molecules from evaporating and maintain the structure of a hydrogel, techniques such as encapsulation by an elastic substrate and solvent replacement are employed [68]. Previously, the authors have proposed a novel gelatin-based shape sensor for flexural soft robots[91] . As the concept is proven in the previous work, in the current study, a three-chamber sensor is fabricated and tested to enhance further the detection of the direction of forces and torsion.

3.2 Contributions

This study aimed at developing a soft embedded tri-axial force sensor capable of being structurally integrated with soft robots. The study contributes to 1) the development of highly accurate force sensors for soft robots, 2) the development of a learning-based calibration schema as an extension of previously analytical calibration schema, and 3) capturing the intrinsic rate-dependency of soft sensors through deep neural calibration with temporal rates of sensor voltages.

3.3 Materials and Methods

3.3.1 Sensing Principle and Design

The proposed sensor's sensing method is based on the discovery of a nonlinear relationship between the deformation-induced changes in the electrical resistance of a soft sensor. To be suitable for soft robotics applications, the sensor's stiffness must be comparable to that of the robot in order to minimize deformability loss due to the sensor's addition. Given that soft flexural robots are often constructed of soft elastomers, particularly for surgical applications, the stiffness of the sensor should be minimal [108]. As a result, the authors have suggested and shown the performance of an extremely soft gelatin-based shape sensor for flexural robots in this work.

The proposed sensor's sensing method is based on the discovery of a nonlinear relationship between the deformation-induced changes in the electrical resistance of a soft sensor. To be suitable for soft robotics applications, the sensor's stiffness must be comparable to that of the robot in order to minimize deformability loss due to the sensor's addition. Given that soft flexural robots are often constructed of soft elastomers, particularly for surgical applications, the stiffness of the sensor should be minimal [108]. As a result, the authors have suggested and shown the performance of an extremely soft gelatin-based shape sensor for flexural robots in this work.

To demonstrate how the theory works, we constructed and tested a single-chamber sensor. While the single-chamber sensor has a relatively average inaccuracy of 4%, our past study indicates that it is unsuitable for measuring the direction of force and torsion. Increased sensing nodes, improved sensor combinations, and novel reconstruction algorithms are all approaches to increasing soft robotic perception accuracy [109]. As a result, we designed a multi-chamber sensor to provide a more precise measurement of the force's direction.

Fig. 3.2 shows the flexure's schematic geometrical design and fabrication process. This form of the flexural body is one of the most straightforward constructions for soft robots and has been extensively used in medical applications, e.g., [110]. The flexural body had a central blind cylindrical chamber that acted as a mold for the suggested gelatin-based sensing element, which consisted of three chambers. Additionally, during the molding process, two copper wires were put at the bottom and top of each chamber, which was employed in a voltage divider to measure the voltage differences between them. This design enabled for encapsulation of the sensing element within the flexure, alleviating worries regarding the sensing device's acute biocompatibility.

Due to the piezoresistance of the gelatin-graphite composites, their electrical resistance varies when deformed. This phenomenon may be attributed to variations in the effective diameter and length of the sensing element caused by deformation within the soft body. The primary mechanism of deformation in flexural soft robotics is bending, and the parameters of importance in soft robotic applications are the bending angle [31] and tip forces [111]. Thus, the modeling purpose was to determine the connection between the sensing element's electrical resistance and bending angle, as well as torsion.

The sensing element's resistance R was modeled as a function of its particular resistivity ρ, cross-sectional area A, and length L. Prior to deformation, the sensing element's specific resistance ρ was determined using its initial resistance $R_\circ$:

$$R_\circ = \rho \frac{L_\circ}{A_\circ}, \tag{11}$$

Twisting and bending deformation alters both L and A due to the longitudinal strain induced along the sensor element. Due to the sensing element's high water content and elastomeric nature, its cross-sectional area would necessarily decrease to compensate for its longitudinal elongation. Thus, during deformation, the sensing element's resistance would be:

$$R = \rho \frac{L}{A}, \tag{12}$$

The incompressibility requirement required: Assuming an infinitesimally tiny sensing element, dS as the initial length of the differential element, and ds as its deformed length, the incompressibility constraint required:

$$Ads = A_\circ dS \Rightarrow A = A_\circ \frac{dS}{ds} \tag{13}$$

Given that deformation of the flexural robot is a complex nonlinear function of external load, analytical determination of $\frac{dS}{ds}$ might be impossible. Nevertheless, this theoretical derivation elaborates on how the sensing principle works and shows how external force components in 3D may influence changes in the resistivity of sensing elements in the chambers. In addition, the term $\frac{dS}{ds}$ might be a temporal function of external load and dependent on the time history of force. Thus, it may introduce hysteresis. Therefore, in the following, the authors have proposed a nonlinear rate-dependent calibration model that could capture the geometrical and temporal nonlinearities of the proposed sensor.

3.3.2 Fabrication

The manufacturing procedure for the soft body and soft sensor is depicted in Fig 3.2. To construct the soft body, and a cylindrical mold was printed using polylactide acid (PLA) filaments on a 3D printer (Replicator+, MakerBot, NY, USA). Ecoflex 50 was created by combining equal parts A and B. To achieve homogeneity, the mixture was agitated for 5 minutes. The mixture was degassed for ten minutes under 30 in-Hg vacuum pressure. Following injection into a 3D-printed mold, the slurry was allowed to be set for two hours at $25°C$. The soft sensing element was synthesized by infusing gelatin with graphite microplatelets (Graphinox, India). As seen in Fig 3.2, the gelatin sachets were steeped for 2 minutes in $10°C$ water. After soaking the sachet in 50 mL of hot water, it was transferred and swirled until fully dissolved. After adding 5mL graphite microplatelets to the solution, the emulsion was agitated to bring it to room temperature. After injecting the emulsion into the chamber of the soft body using a 10mL injection syringe, two copper wires were previously put and fastened into each chamber. The soft body was then held at $4°C$ for two hours to solidify the gelatin. After setting, the injection site on the chambers was sealed, and the soft sensor was encapsulated with Ecoflex. The entire encapsulation of the gelatin-based sensor after setting at $4°C$ was also critical to preventing gelatin from melting at ambient temperature since its confinement in Ecoflex prevents volumetric variations in gelatin required for melting.

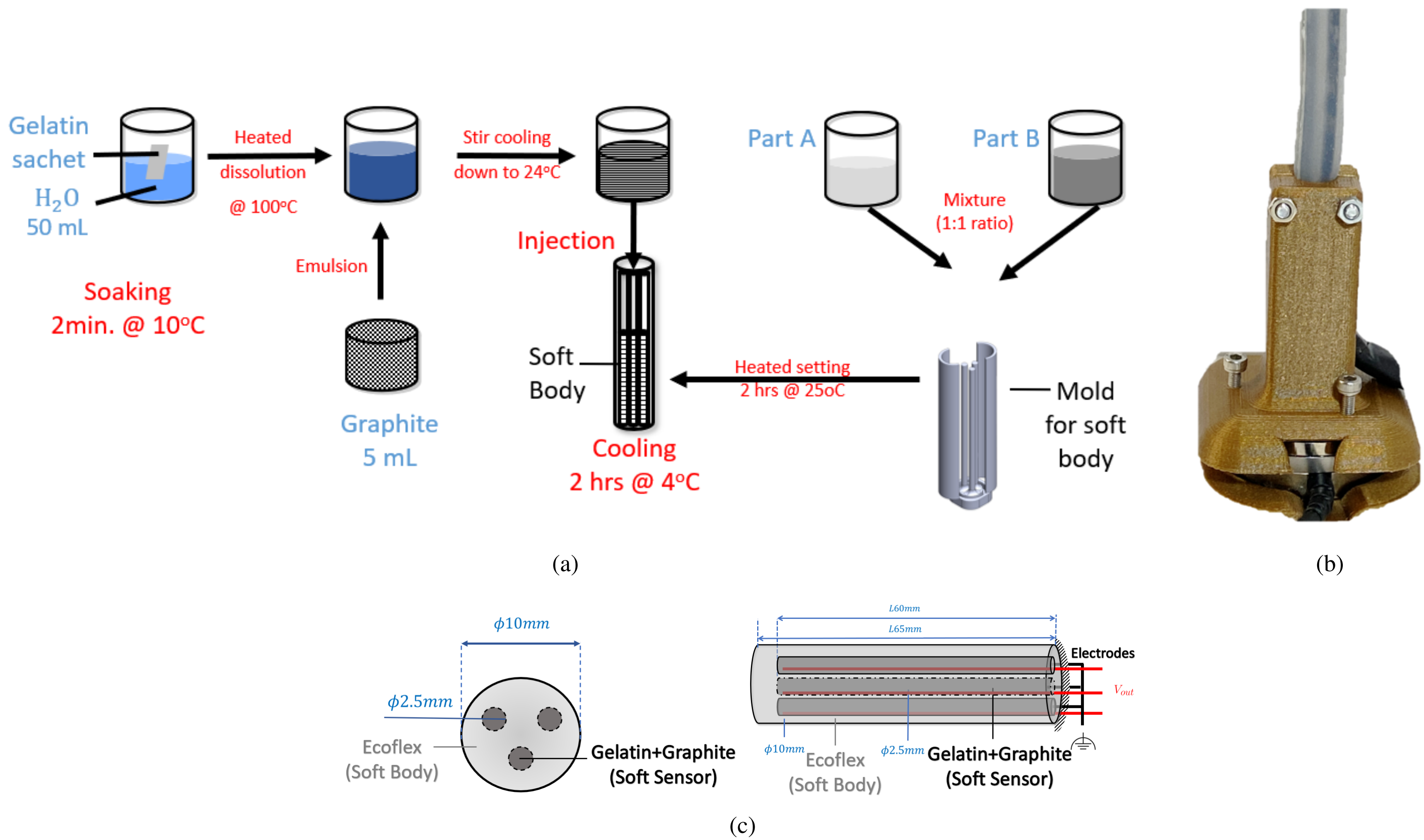

Figure 3.2: (a)Schematic process flow of fabricating the sensing element, i.e., gelatin-graphite composite., (b) prototyped sensor embedded in a soft flexure, and (c) geometric design of the sensor and flexure.

3.4 Neural Calibration and Validation

3.4.1 Test Protocol and Setup

The soft sensor was mounted on a 3D-printed platform housing. After that, the platform was attached to an ATI mini40 force/torque sensor (ATI Industrial Automation, NC, USA). The experimental design for this investigation is depicted in Fig. 3.3(a). The force applied to the sensor was measured using the ATI sensor. Meanwhile, the voltage variations in the sensor were measured using an Arduino Uno. The sensor was serialized and each channel connected to a +5v excitation through a 300Ω resistor to create a voltage divider circuit. The result of bending and twisting the soft sensor is explained in the following section.

3.4.2 Learning-based calibration

The Arduino Uno measured voltage changes in the chambers, while the ATI mini40 force sensor measured force in three directions. Additionally, because of the time-dependent nature of gelatin's characteristics, the gradient of voltage in each chamber with respect to time is evaluated for further study. A training dataset of 12000 data samples obtained in the calibration experiment, a dataset with six inputs, i.e., voltage changes of the chambers $\begin{pmatrix} V_1 & V_2 & V_3 \end{pmatrix}^T$ and their temporal rates $\begin{pmatrix} \dot{V}_1 & \dot{V}_2 & \dot{V}_3 \end{pmatrix}^T$, and three outputs, $\begin{pmatrix} F_x & F_y & F_z \end{pmatrix}^T$ was constructed. A deep neural network with one input layer (6 neurons), five hidden layers (250,150,100,50,10) neurons, and one output layer (3 neurons) was trained with the training dataset in Python3.9 using the Scikit-learn package. The training dataset was split with a 70:30 train-to-test split ratio. The network's neurons were coupled with 'tanh' activation function to preserve the inputs' sign. Also, the 'adam' solver with a learning rate of 0.001 was chosen for training.

The results of the training showed that the proposed calibration had a goodness-of-fit of R^2 =0.98 with a mean absolute error of 0.005 N. Fig. 3.3(b) depicts the measured force used in the calibration of the sensor. Also, Fig. 3.4 shows the variation of ΔV_1, ΔV_2, and ΔV_3 with external forces. As can be seen in Fig.3.4, external forces, F_x, F_y, and F_z, have distinct effects on the variation of

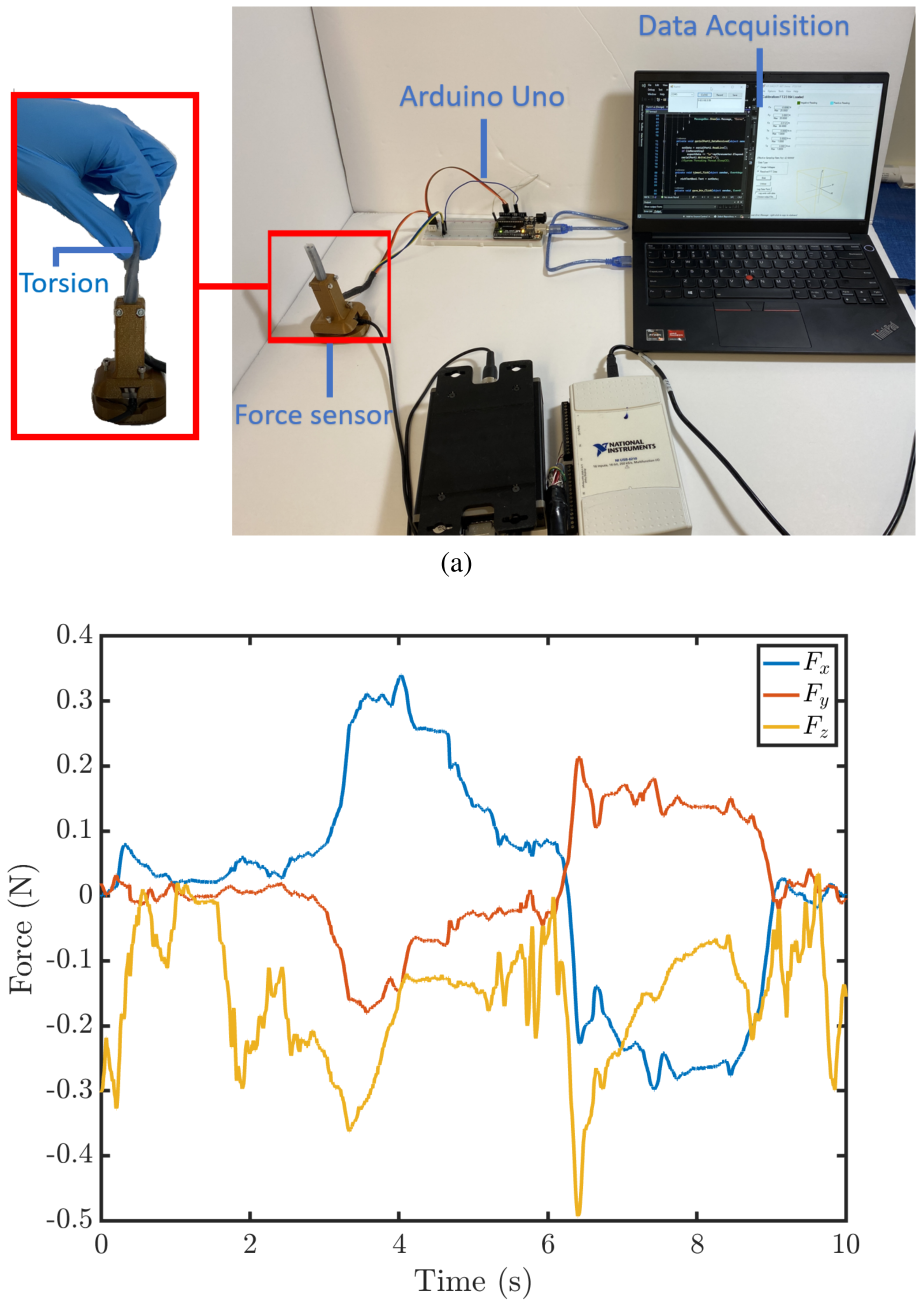

(a)

(b)

Figure 3.3: (a) Test setup for calibration and experimental validation, (b) external forces measured during calibration test.

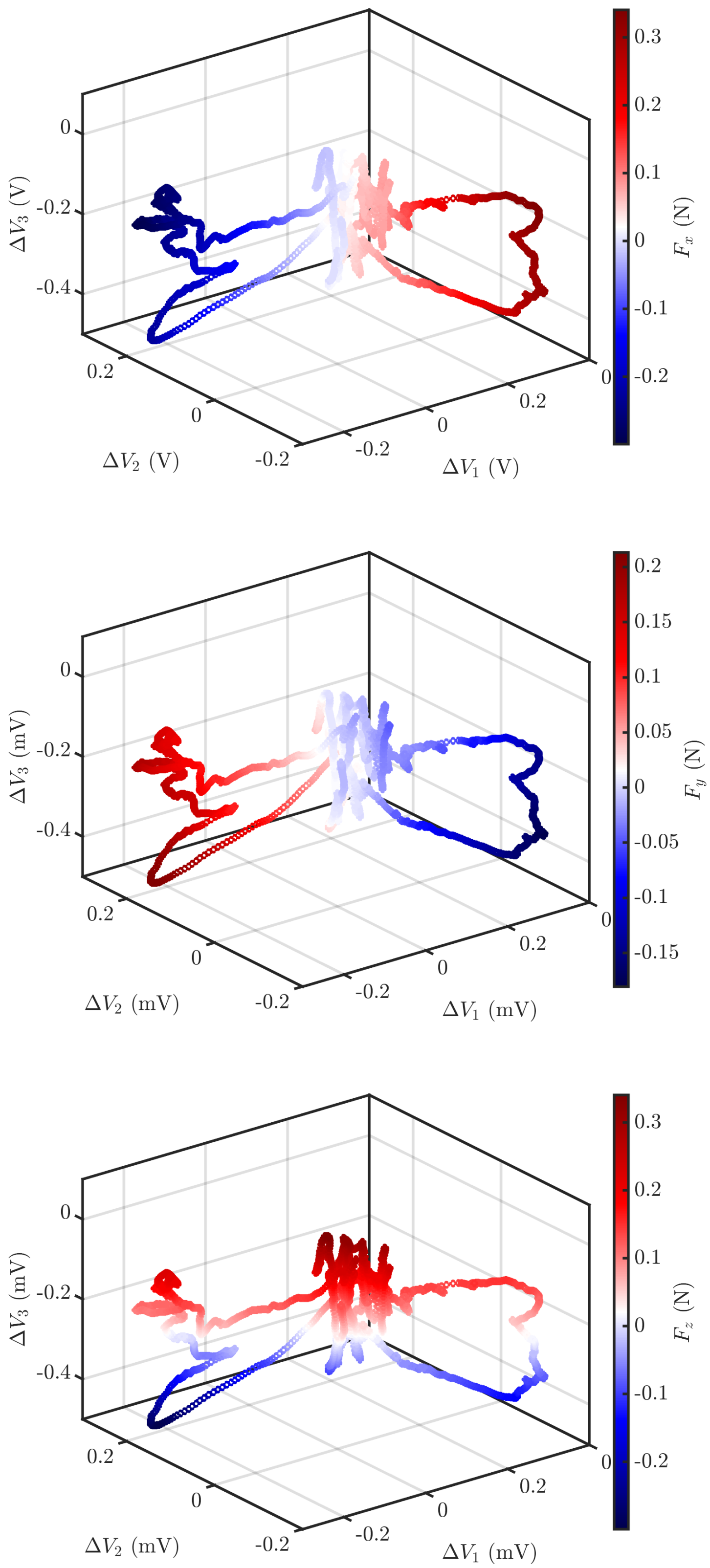

Figure 3.4: Variation of voltages with external forces used in calibration.

voltage in each chamber. Nevertheless, the results showed that there is significant nonlinear cross-talk between the voltages such that the effects of F on V-s could not be decoupled. A similar phenomenon was observed amongst the temporal rates of voltages. This observation justifies the selection of a rate-dependent and nonlinear calibration method.

3.4.3 Experimental validation

In a second experiment, the calibrated sensor was used with the same setup as shown in Fig. 3.3 to compare the real-time estimated forces obtained with the calibration model (predictions) with ground truth forces obtained from ATI force sensors (reference). The calibrated model was deployed on a Windows application (C# programming language) and was fed with voltage measurements. The predictions and reference forces were recorded for post-processing.

Fig. 3.5 compares the reference and prediction for three external force components, while Fig. 3.6(a-c) shows the correlation between the reference and predicted force components. The results showed that a mean-absolute error of 0.007 ± 0.005 N, 0.008 ± 0.006 N, and 0.011 ± 0.008 N for F_x, F_y, and F_z, respectively. The results showed high linearity between the predictions and reference forces (Fig. 3.6(a-c). The 99% confidence interval ($\pm 3 \times standard - deviation$)) was bounded in $[-0.05, +0.05]$N for all the force components with a normal distribution without significant skewness. Numerical analysis of the estimated forces showed that the smallest detectable change in external force with the proposed sensor was 0.003 N across the three force components. This indicates a force resolution of 0.003 N for the proposed force sensor. Moreover, given that the proposed force sensor outputs were closely following the reference force both in loading (increasing forces) and unloading (decreasing forces), the hysteresis phenomenon was not evident in the sensor output. Given that hysteresis was an intrinsic property of the soft body [32], the proposed rate-dependent calibration model was successful in capturing it through the inclusion of voltage rates as input features. Typically, the range of external forces acting on soft sensors depends on their application. For example, for soft robots used in minimally invasive cardiac surgery, external forces are within the 0.2 N range with a resolution of down to 0.005 N [32]. The proposed force sensor exhibited an acceptable force measurement range (± 0.3 N) and resolution of 0.003 that meet the requirements of surgical applications, such as cardiac surgery. Also, the proposed encapsulated

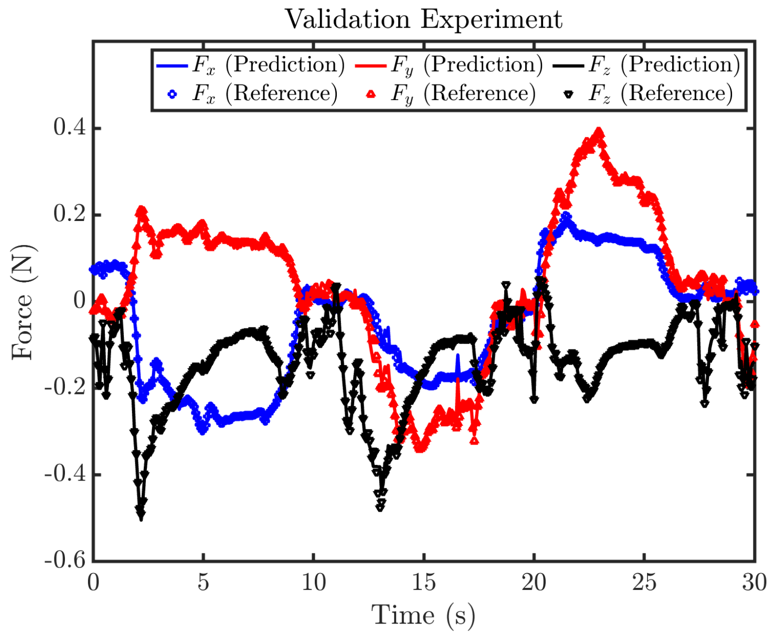

Figure 3.5: Comparison of predicted and reference force components in the validation test.

design of the sensing elements into the soft body allows for mitigating the risk of contamination of biological tissues with sensing materials.

3.5 Summary

In this study, a soft sensor with an embedded design into a soft flexure (soft robot) was proposed, prototyped, calibrated, and validated. The proposed sensing element is moldable, thus allowing for shape variability to meet application requirements. Also, the proposed rate-dependent calibration allowed for capturing hysteresis and contributed to the high accuracy of the proposed sensor. A future expansion of this study could be to use the proposed sensor in a miniaturized surgical instrument or soft robotic surgical device. Also, the utilization of different polymers instead of gelatin could contribute to strengthening the sensor, thus increasing its force measurement range. Another expansion of this study could be to embed the sensing element in a feedback control system with a soft sensor to study its performance for practical control applications.

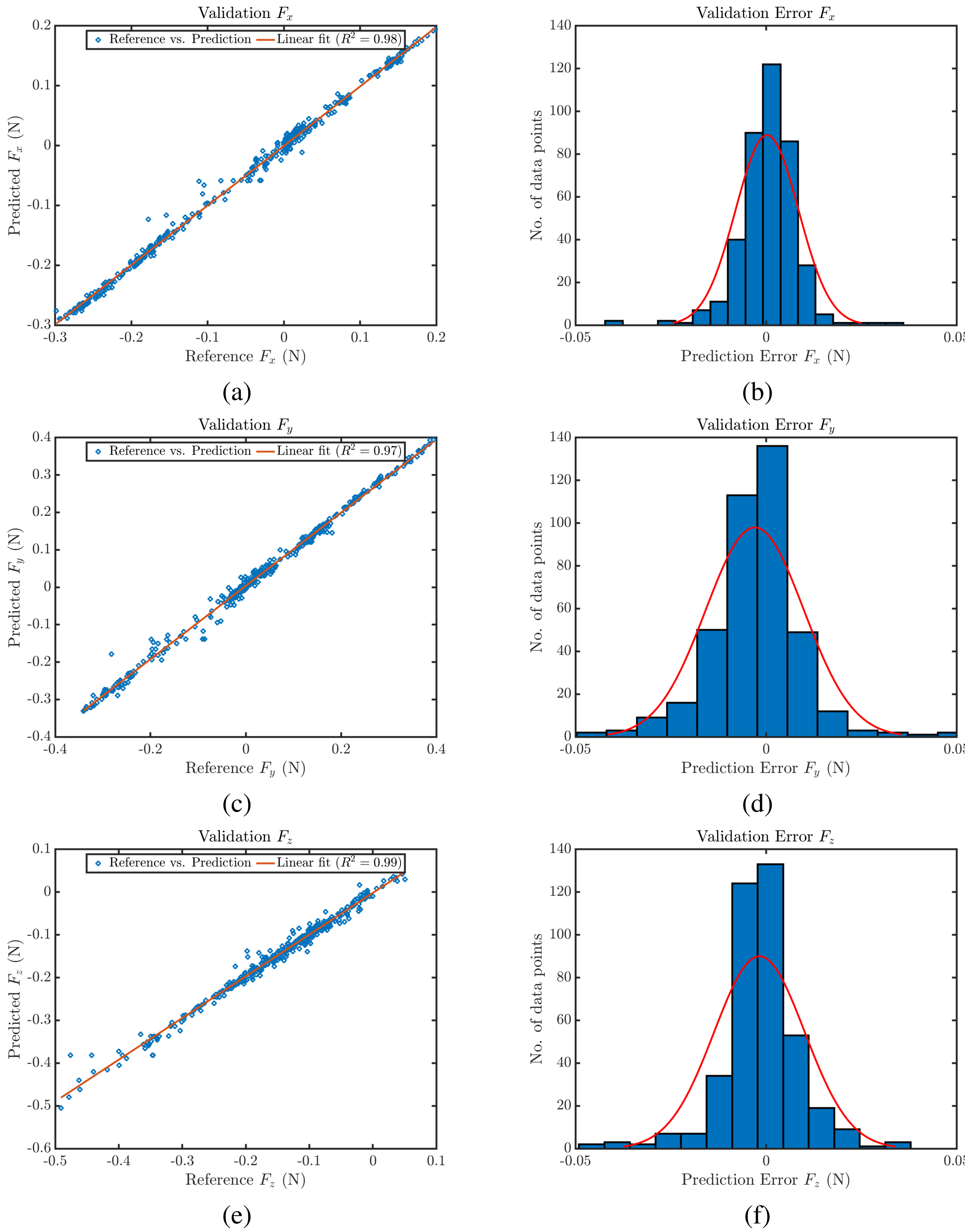

Figure 3.6: (a,c,e) Comparison of the reference and predicted external forces, and (b,d,f) distribution of prediction error with normal distribution fitting.

Chapter 4

Embedded Six-DoF Force-Torque Sensor for Soft Robots with Learning-based Calibrations

Soft robots typically exhibit large deformation that makes integration of rigid sensors with them cumbersome. Especially for soft surgical robots, direct sensor-based feedback is required. In this study, we have proposed, modeled, prototyped, and validated a novel smart polymer-based soft sensor for integration with soft robots. Previously we have shown that the proposed smart polymer exhibits piezoresistivity. Thus, in this study, we integrated the proposed sensor with a flexural soft robot. Afterward, the sensor was calibrated through a series of experimental tests, and a multi-layer perceptron was trained for the calibration. The calibration showed a maximum root-mean-square error of 10.6 mm and a mean absolute error of 8$\pm$10 mN compared with the ground truth. The experimental validation showed that the proposed sensor and calibration method demonstrated a combined mean absolute error of 7.4$\pm$6.5 mN. In addition, the minimum detectable force of the sensor was less than 1 mm, with a range of up to 284 mm. The system performance was compatible with the range and accuracy requirements of representative intraluminal applications.

4.0.1 Related Studies

Fig. 4.1 depicts a representative intraluminal use case for soft sensors. The piezoresistive effect that some classes of materials experience following elastic deformation serves as the foundation for the operation of piezoresistive sensors. Universally acknowledged as being the most frequently utilized equipment at both the micro- and macro-scales [112, 113]. Resistive tactile sensors are made up of active materials placed between two opposing electrodes or placed on a pair of in-plane electrodes. Active materials are typically composites formed of conductive components and a matrix. When force is exerted on the sensor, the connections with conductive materials in a porous matrix or the surface between the conductive materials and electrodes expand, significantly lowering the resistance. The composition and geometric design of the active material are essential drivers of the tactile sensor's performance because it acts as both an electrical channel for current flow and a flexible structure throughout the operation [26].

Due to their exceptional electrical conductivities and distinctive nanoscale flexibility, graphene-based piezoresistive sensors are particularly appealing [79]. Highly flexible and sensitive sensors have been created using graphene-based microstructures since graphene has been assembled in various forms of two-dimensional (2D) or three-dimensional (3D) macroscopic, freestanding constructions using a few distinct processes [80]. By introducing flexible polymer into 3D graphene frameworks or uniformly dispersing graphene sheets within flexible polymer matrices, graphene/flexible matrix composites were created [81]. Due to their greater flexibility, flexible polymers like polydimethylsiloxane (PDMS), Ecoflex, polyimide (PI), and polyurethane (PU) are frequently employed as substrates or matrices [82]. Moreover, Due to their distinctive structural interconnectivity, high porosity, and stable mechanical properties, 3D graphene architectures, such as foams, hydrogels, aerogels, and sponges, were simple to infiltrate with liquid polymers [83, 84]. Incorporating hydrogen and graphite produces self-healing properties. For flexible devices that may be included in fully functional applications, intrinsic self-healing based on molecular interactions with quick and reversible healing capabilities, such as hydrogen bonding, is preferable to extrinsic self-healing for strain sensors [85].

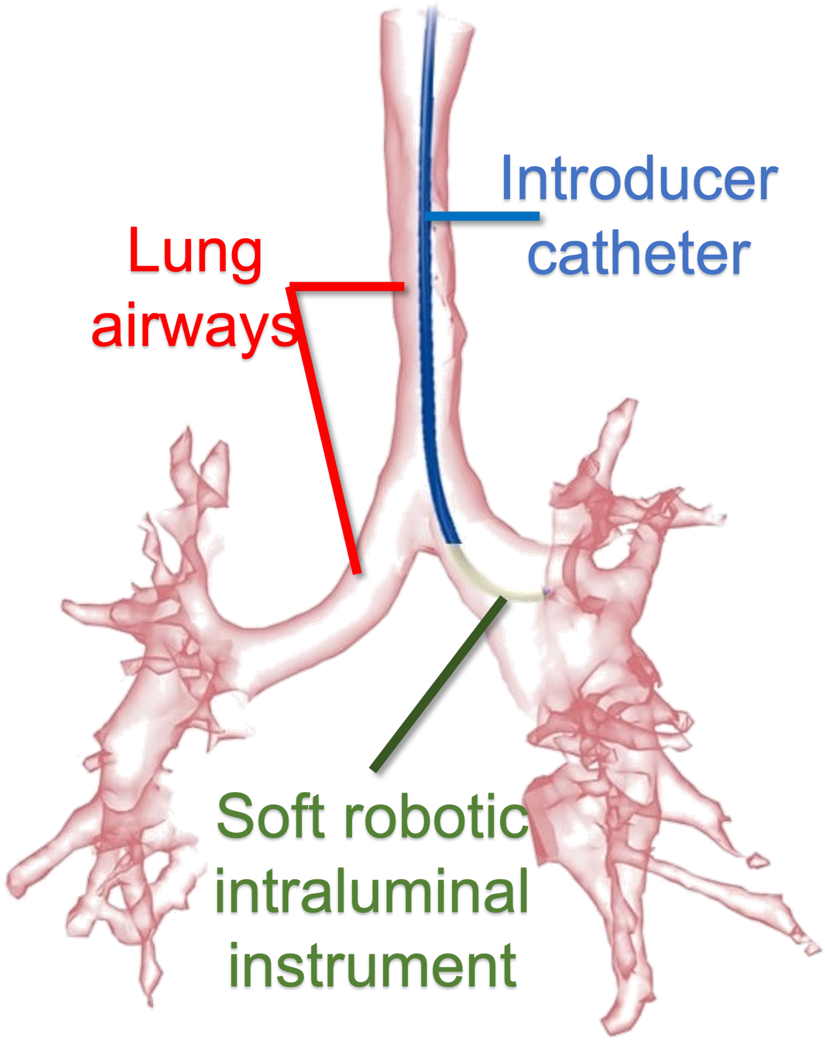

Figure 4.1: Schematic depiction of using sensor-embedded soft sensors for bronchoscopy procedure.

4.1 Requirements

The functionality of sensors used in portable electronic devices should not be confined to a single stimulus operating alone, such as strain, twist, or pressure [87]. Widespread applications in multiple-degrees-of-freedom environments require multidimensional sensors capable of sensing complicated multiaxial strains. Creating conductive networks with an anisotropic structure is one method for designing multidimensional sensors capable of sensing multiaxial strains [88]. In the author's prior research, gelatin and graphite were used as a piezoresistive sensor encapsulated in

PDMS to create a soft sensor. Gelatin has self-healing characteristics, and its combination with graphite increases the resistance range. The proposed sensor was modeled, and its model was experimentally validated. The sensor's performance demonstrated its compatibility with the range and resolution requirements for surgical applications of soft robotics. Instead of a single straight chamber, we utilized a moon-shaped chamber with more than two electrodes to measure forces in three directions and torsion in the current study. In addition, Ecoflex was employed as the soft body instead of PDMS, allowing the sensor to be more flexible and deformable.

4.2 Sensor Design and Modeling

4.2.1 Sensing principle

Although stiff structures provide more precision, their restricted flexibility and relatively large diameter are the main challenges for MIS in expanding operation space and reducing trauma during surgeries [114]. Soft robots, as opposed to hard-bodied robots, have bodies composed of intrinsically soft and/or extensible materials (such as silicone rubbers). These robots have a continuously elastic structure with muscle-like actuation that mimics biological systems and results in a comparatively high degree of freedom as compared to their hard-bodied competitors[115]. Because soft flexural robots are often composed of soft elastomers, particularly for surgical applications, the stiffness of the sensor must be minimal [31]. As a result, in this study, both PDMS and Ecoflex are used as materials to represent the body of the housing. Additionally, the gelatin and graphite combination serves as an internal piezoresistive sensor within the soft body. Fig. 4.2(a–b) depicts the flexure's geometrical design and schematic wiring of the electrodes inside the sensing element, and Fig. 4.2(c) shows a simplified equivalent electrical model of the sensing element in a voltage-splitting configuration for data acquisition. In the schematic, V_e and R_e correspond to the voltage measured by the electrode at the end (tip) of the sensor and the total electrical resistance of the sensing element. Also, $V_\circ$ is the pull-up voltage used as the stimulator of the voltage splitter circuit, and R_c is a constant resistor used for voltage splitting. The second design's goal is to miniaturize the sensor based on the current size of MIS applications and to enable 3 degrees of freedom sensing by increasing the number of electrodes, as the first design demonstrates the feasibility of the sensing

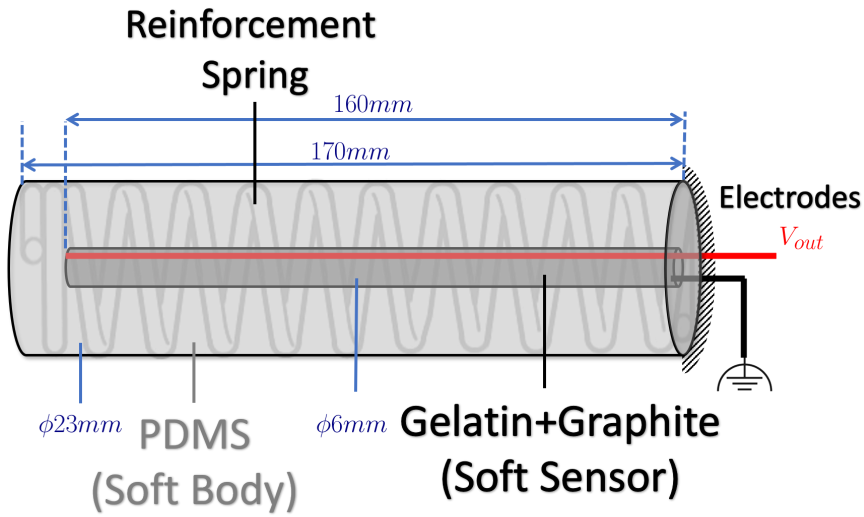

(a)

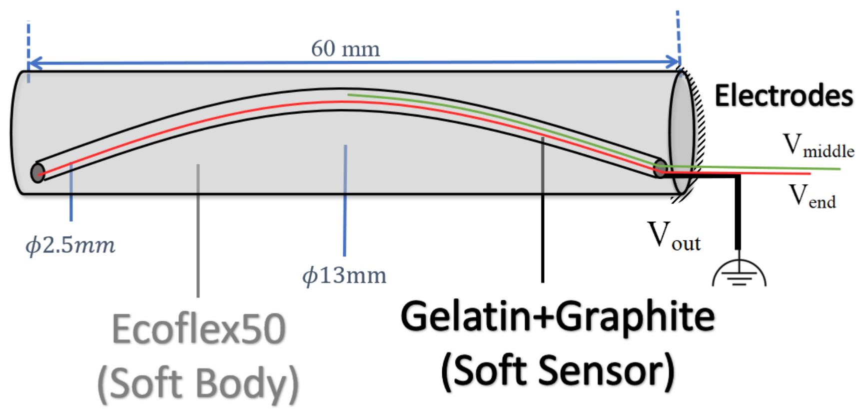

(b)

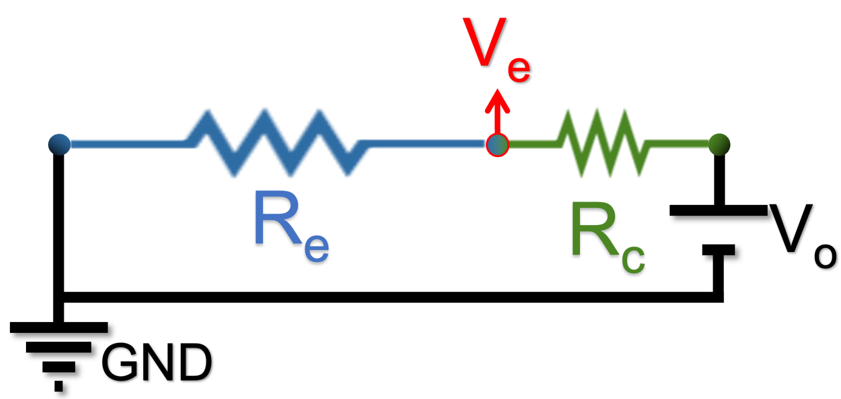

(c)

Figure 4.2: (a) The structural design of the sensor with gelatin/graphite capsulated inside PDMS, (b) Enhanced design of the sensor with gelatin/graphite capsulated inside Ecoflex50, (c) simplified electrical model of the sensor and voltage splitter circuit.

principle. This type of flexural body is one of the most basic structures for soft robots, and it has been widely used in medical applications [42].

The central blind cylindrical chamber of the flexural body served as a mold for the proposed gelatin-based sensing element. One has a single straight chamber as a one-degree-of-freedom shape sensor, while the other has a single moon-shaped three-degree-of-freedom force sensor. During the molding process, copper wires were also placed, which were used in a voltage divider to measure the voltage differences between them. This design allowed for the encapsulation of the sensing element within the flexure, which alleviated concerns about the graphite used in the sensing element's acute biocompatibility.

4.2.2 Fabrication

The fabrication process for the soft body and soft sensor is shown in Fig. 4.3. A cylindrical mold was created using polylactide acid (PLA) filaments and a 3D printer (Replicator+, MakerBot, NY, USA) to prepare the soft body. For the first sample, the Ecoflex 00-50 (Smooth-On Inc., PA, USA) was mixed in a 1:1 ratio for parts A and part B [116]. To achieve homogeneity, the mixture was stirred for 5 minutes. The mixture was degassed for 10 minutes under 30 in-Hg vacuum pressure. After that, the mixture was injected into a 3D-printed mold, and the coil spring was placed inside. After that, the mold was left to set for 24 hours at $25°C$.
Gelatin was impregnated with graphite microplatelets to make the soft sensing element (Graphinox, India). As demonstrated in Fig.4.3, The gelatin sachets were steeped for two minutes in water at $10°C$. The soaked sachet was then transferred to 50 mL of hot water and thoroughly dissolved by stirring. After adding 5mL graphite micro-platelets to the solution, the emulsion was cooled to room temperature while being agitated. Using a 10mL injection syringe, the emulsion was subsequently injected into the soft body's chamber after copper wires had been introduced and fastened within the soft body. The soft body was then maintained at $4°C$ for two hours until the gelatin solidified. After the injection site on the chamber had hardened, the second layer of the soft body was applied to encase the soft sensor. Total encapsulating of the gelatin-based sensor after setting at $4°C$ was also necessary to prevent gelatin from melting at normal temperature, as confinement with the soft body prevents volumetric changes in gelatin that are required for melting.

4.2.3 Modeling and Mechano-electrical Simulation

The piezoresistivity of the gelatin-graphite composites causes their electrical resistance to vary during deformation. This phenomenon may be attributable to deformation-induced changes in the effective diameter and length of the sensing element within the soft body. In flexural soft robotics, bending is the predominant mode of deformation, and bending angle [117] as well as and lateral tip forces [105, 104] are the metric of importance in soft robotic applications.

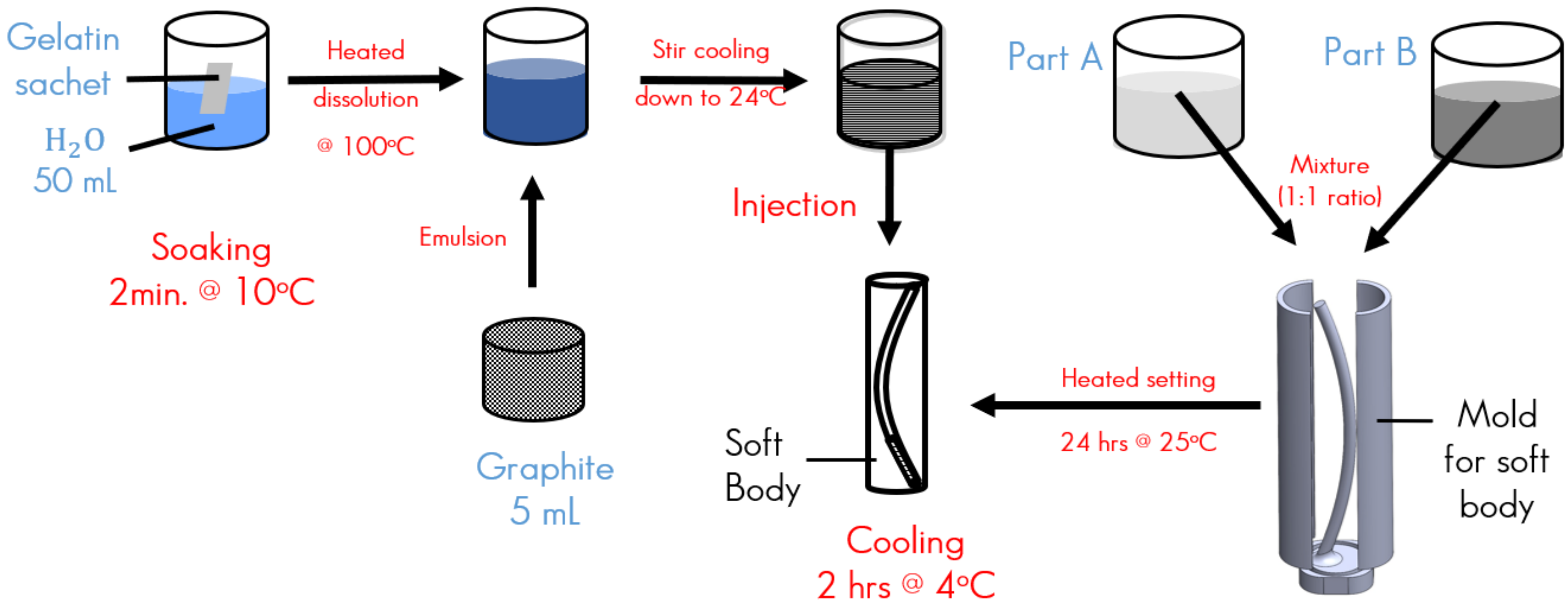

Figure 4.3: Fabrication of gelatin and graphite mixture inside Ecoflex layer.

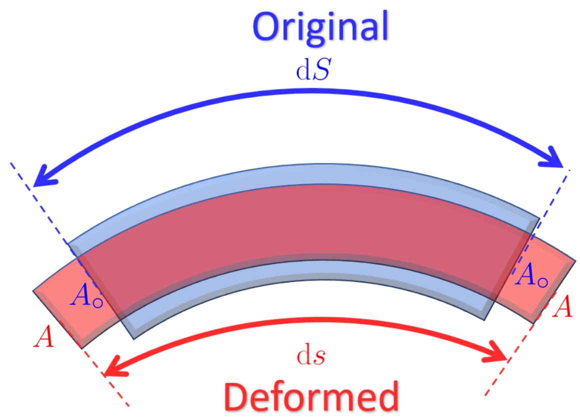

Figure 4.4: Differential element of the sensing element under deformation.

In a prior model-based investigation, the link between the electrical resistance of the sensing element and the bending angle was studied. Experiment findings were utilized to validate the model. In the present investigation, finite element studies were utilized to determine the bending angle for three force directions. The goal of the modeling was to establish a connection between the electrical resistance of the sensing device and the bending angle.

The sensing element's resistance R was modeled as a function of its specific resistivity ρ, cross-sectional area A, and length L. Prior to deformation, the specific sensitivity ρ of the sensing element was derived from its initial resistance $R_\circ$:

$$R_\circ = \rho \frac{L_\circ}{A_\circ}, \tag{14}$$

As bending deformation produces strain along the sensing element, L and A will change. Since it was expected that the sensing element was incompressible due to its high water content and elastomeric nature, the sensing element's cross-sectional area would unavoidably decrease to compensate for its longitudinal elongation. Consequently, the resistance of the sensing element during deformation would be:

$$R = \rho \frac{L}{A}, \tag{15}$$

Fig. 4.4 contrasts the deformed and original forms of an infinitely small sensing element. With

dS as the differential element's original length and ds as its deformed length, the incompressibility condition required:

$$A ds = A_\circ dS \Rightarrow A = A_\circ \frac{dS}{ds} \tag{16}$$

When force F is applied to the tip of the sensor, it bends. Thus, the sensing element structurally goes under a distribution of strain that causes a spatial distribution of length and diameter along its length. To simplify the mathematical problem, F_x is first applied to the sensor, as shown in Fig 4.9. According to continuum mechanics, the longitudinal stretch λ for a 1D differential element subjected to bending-induced elongation is as follows:

$$\lambda = \frac{ds}{dS} = \frac{L}{L_\circ}, \tag{17}$$

Hence, Eq. 16 was simplified to:

$$A = A_\circ \lambda^{-1} \tag{18}$$

For a given deformed length L, the mechano-electrical model would therefore predict an electrical resistance of:

$$R = \rho \int_0^L \frac{ds}{A}. \tag{19}$$

Changing distorted Eulerian coordinates to original Lagrangian coordinates simplifies the integral to:

$$R = \rho \frac{1}{A_\circ} \lambda^2 \int_0^{L_\circ} dS = R_\circ \lambda^2 \tag{20}$$

Consequently, the sensing element's resistance would fluctuate quadratically as a result of the nonlinear stretch generated by significant bending.

4.2.4 Model Verification

To verify the derived model, the length change of the sensing element under a representative loading situation was simulated using the finite element approach, and the computational stretch was utilized to forecast the change in the sensing element's resistance. In order to accomplish this, the sensor's geometric model Fig. 4.2(b) was imported into Abaqus (R2021, Dassault Systemes, France) and meshed with tetrahedral meshes. Models of hyperelastic materials were utilized for both the soft body and the sensing element. The mesh size (n=28,000 tetrahedral elements) was determined using a mesh-independence test on the model's total strain energy. The base of the soft body and the sensing element was also subjected to Dirichlet and Neumann boundary conditions. The tip of the soft body was subjected to a half cycle of forces extracted from a verification experiment.

In three separate simulations, maximum tip forces of 70, 40, and 70 mN were applied on the soft body in FEM in x, y, and z (compression) directions, respectively. Similar forces were applied experimentally on the prototype sensor while the temporal variation of sensing element voltages (V_m and V_e) were recorded for comparison with model predictions based on the FEM results. Table. 4.2 presents the material models used in FE simulations. Fig.4.6 depicts the simulated deformation of the soft body and sensing element under the representative loadings taken from the experiment. Fig. 4.5 compares the variation of stretch along the sensing element with $F_x = 70$ mN with 25%, 50%, 75%, and 100% load.

To verify the model, first, the stretch from FEM models was obtained offline. Afterward, numerical integration on the longitudinal stretch (λ) as a function of undeformed coordinates S was performed using the 4th-order Runge-Kutta method. Eq. 22 is basically a differential extension of Eq. 20. integrated to obtain the total change in length.

$$R_m = R_\circ \int_0^{\frac{L_\circ}{2}} \lambda^2(S) \mathrm{d}S \tag{21}$$

$$R_e = R_\circ \int_0^{L_\circ} \lambda^2(S) \mathrm{d}S \tag{22}$$

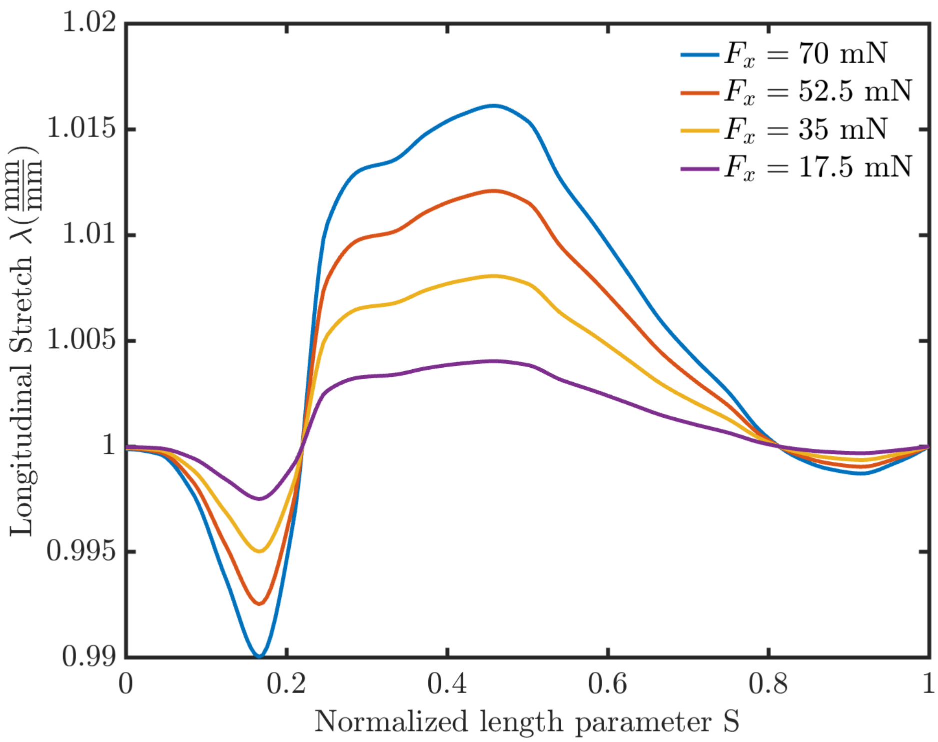

Figure 4.5: Variation of stretch along the sensing element in three simulation loadings.

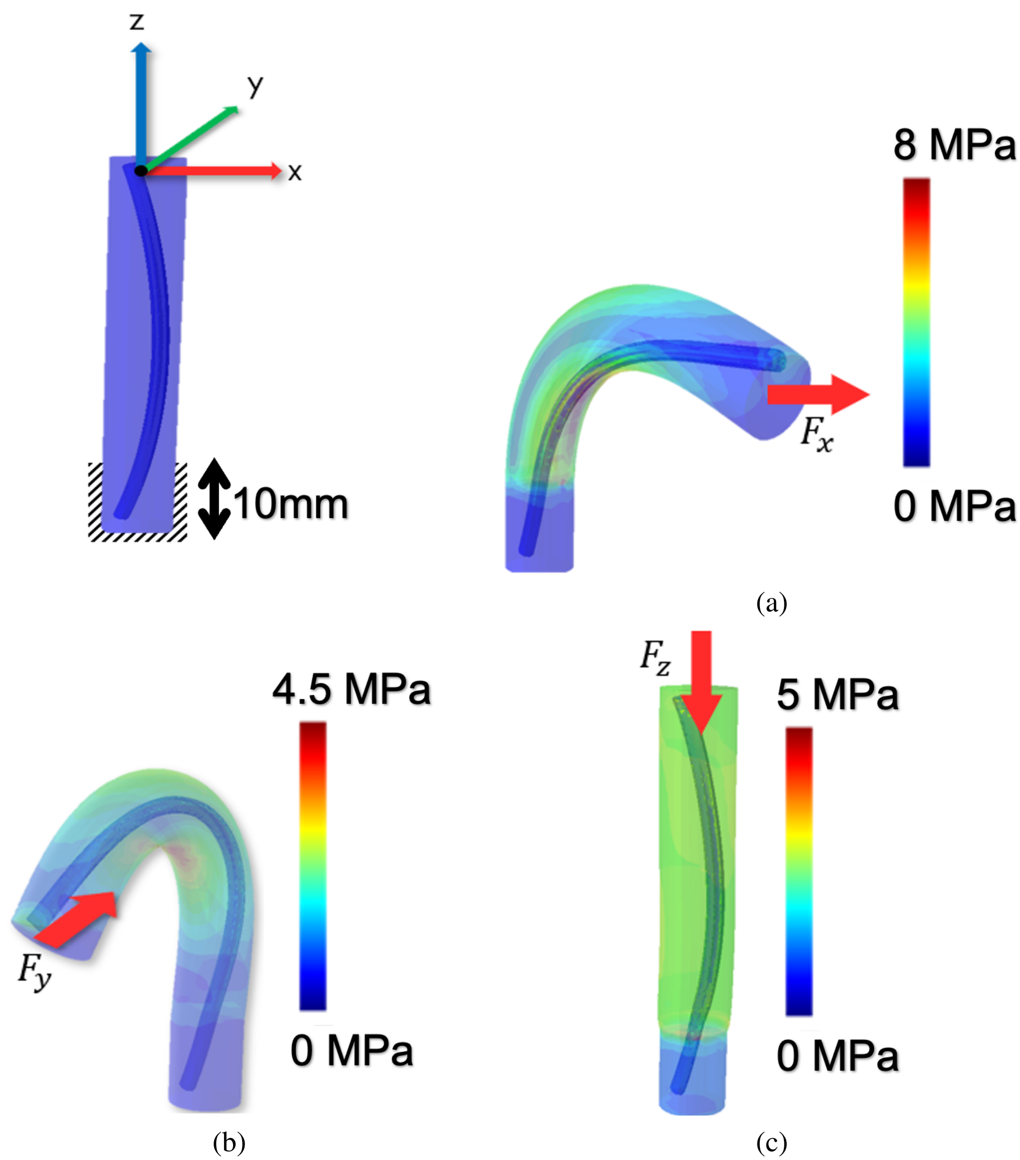

Figure 4.6: Von Mises stress contour of the finite element model for (a) $F_x = 70$ mN. (b) $F_y = 40$ mN, and (c) $F_z = 70$ mN.

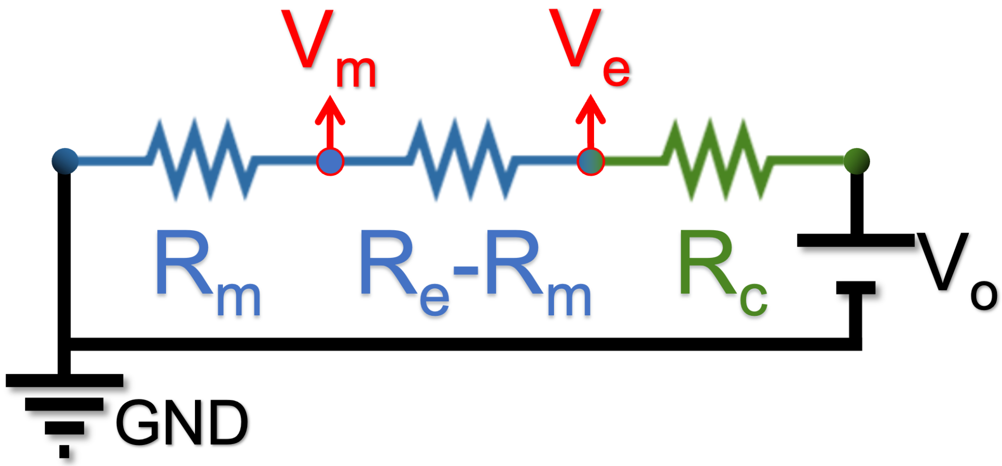

Figure 4.7: Detailed equivalent electrical model of the sensing element with the placement of electrode voltage measurements.

On the other hand, from experimental measurements, at any time, two voltages were recorded corresponding to electrodes installed at the sensor's middle point and end, V_m and V_m, respectively.

Fig. 4.7 shows a simplified electrical model of the sensor in a voltage splitting configuration, with $V_\circ = 5v$ as the pull-up voltage and $R_c = 300\Omega$ as a constant resistor for voltage splitting. From Kirchoff's law of voltage, the recorded V_m and V_e were related to R_m and R_e such that:

$$R_e = R_c \frac{V_e}{V_\circ - V_e} \tag{23}$$

$$R_m = R_c \frac{V_m}{V_\circ} \left(1 + \frac{V_e}{V_\circ - V_e}\right) \tag{24}$$

Table 4.1 presents the comparison between the theoretical relative change in R_m and R_e in load cases shown in finite element simulation (shown in Fig. 4.6).

4.2.5 Material Characterization

Three standard samples of Ecoflex 00-50 rubber and the sensing element were produced in order to determine their mechanical properties. The cylindrical samples had a $D_\circ = 29$mm diameter and a $H_\circ = 12.5$mm height. The samples are prepared using the 3D-printed mold and the fabrication

Table 4.1: Comparison of changes in the theoretical and experimental resistance of the sensing element.

	Case 1 $\begin{pmatrix}70\\0\\0\end{pmatrix}$ mN	Case 2 $\begin{pmatrix}0\\40\\0\end{pmatrix}$ mN	Case 3 $\begin{pmatrix}0\\0\\-70\end{pmatrix}$ mN
Resistance (Model)	430Ω	168Ω	392Ω
Resistance (Experiment)	407Ω	189Ω	421Ω
Absolute Error	23Ω	21Ω	29Ω
Relative Error (% of Ground truth)	5.7%	11.2%	6.9%

Table 4.2: Material models used in numerical simulation

Material	Hyperelastic model	Model parameters
Soft body (Ecoflex00-50)	Two-term Mooney-Rivlin	$C_{01} = -9.00 \times 10^{-3}$ MPa $C_{10} = 3.84 \times 10^{-3}$ MPa
Sensing element (Gelatin+Graphite)	Two-term Mooney-Rivlin	$C_{01} = -5.91 \times 10^{-5}$MPa $C_{10} = 5.61 \times 10^{-5}$ MPa

procedure described in Sec.4.2.2 and were put through their tests in accordance with ISO 7743:2017 [106]. Utilizing a universal testing device (Electroforce 2000, TA Electronics, DE, USA). Each sample was subjected to four triangle compression cycles at a displacement rate of 10 mm/min and a range of 0.625mm to 3.125mm, corresponding to 5% to 25% compressive stresses, respectively. The force and displacement data from the fourth compression cycle were used for analysis because the first three cycles were considered conditioning cycles. The samples' stretch-stress curves were calculated using force (f) and displacement (x) data and fitted using a two-term Mooney-Rivlin model. (Eq. 25) [101]:

$$\sigma = 2(C_{10} + \frac{C_{01}}{\lambda})(\lambda^2 - \frac{1}{\lambda}), \tag{25}$$

where, $\sigma = \frac{4f}{\pi D_\circ^2}$ represents nominal stress in MPa, $\lambda = 1 + \frac{x}{H_\circ}$ represents compressive stretch, and C_{01} and C_{10} represent material properties. The curve fittings were done with Matlab 2021b's Curve-fitting Toolbox (Mathworks, MA, USA). A typical stress-stretch diagram of the Ecoflex00-50 sample with the fitted 2MR model is shown in Fig. With a root-mean-square error (RMSE) of 0.001 MPa, the average goodness-of-fit across all samples was 0.9953 for the Ecoflex00-50.

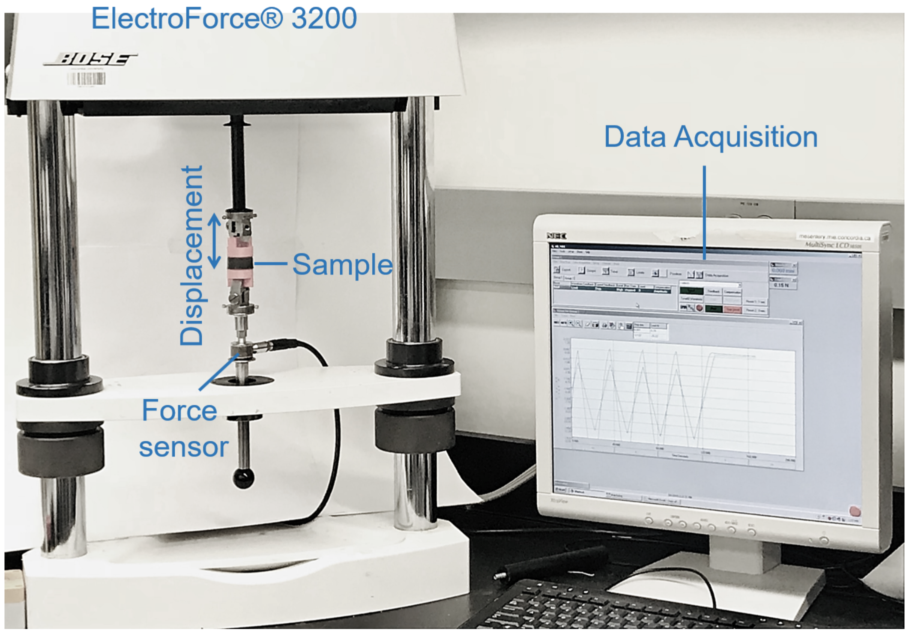

(a)

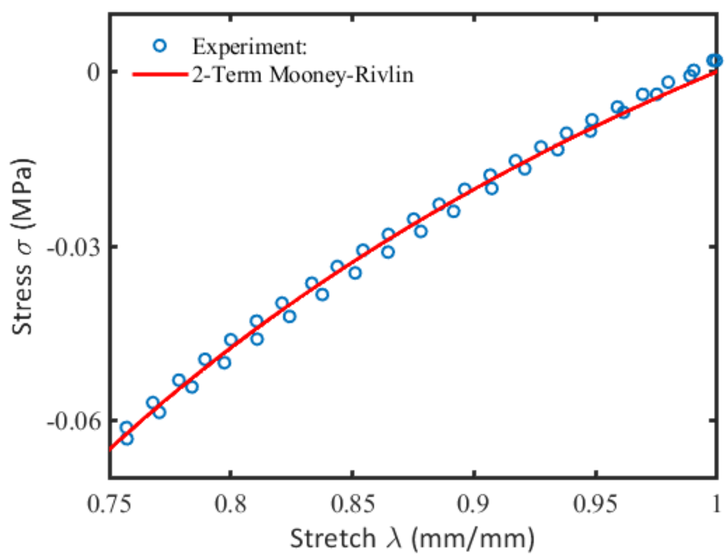

(b)

Figure 4.8: (a) Setup and a representative sample under compression test, (b) a stress-stretch diagram for the Ecoflex00-50 sample.

4.2.6 Sensor Prototype

Fig. 4.9(a) depicts components of the prototype sensor and soft body used in calibration and validation experiments. To prototype the sensor, following the molding of the soft body and soft sensor (summarized in 4.2.2, the body was mounted on a 3D-printed base. After that, the platform was installed on an ATI mini40 force/torque sensor (ATI Industrial Automation, NC, USA). The ATI sensor was merely used for recording ground truth force and torques for *a-posteriori* comparison. The electrodes of the sensing element were connected to an Arduino Uno's analog input channels and were interrogated for voltage at a 250Hz refresh rate. The data was recorded in a PC connected to the Arduino Uno via a serial port. Also, a dedicated user interface and data management software were developed in C# programming language and were used for data acquisition and records-keeping of the project. Moreover, the sensor's calibration model was imported into the user interface and was used for real-time force-torque measurement.

4.3 Neural Calibration

4.3.1 Network architecture

A series of multi-layer perceptron (MLP) neural models were configured for the calibration of the proposed sensor. In our previous study, [91] we showed that a single-layer perceptron could calibrate a single straight chamber force sensor with $R^2 > 0.90$. However, SLP could not exhibit the same performance for force-torque sensing in this study. Thus, we investigated the performance of a series of MLP-s with various hyper-parameters, i.e., the number of hidden layers, learning rates, activation functions, and optimizers. Practically, the proposed neural calibration schema was a regressor relating the voltage readings to the forces acting at the tip of the soft robot. Table 4.3 summarizes the network architectures (number of hidden layers and number of neurons in each layer) and hyper-parameters investigated in this study.

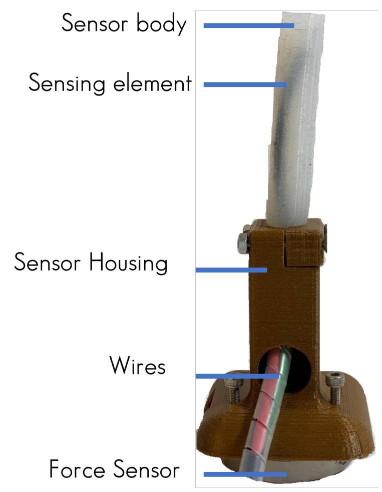

(a)

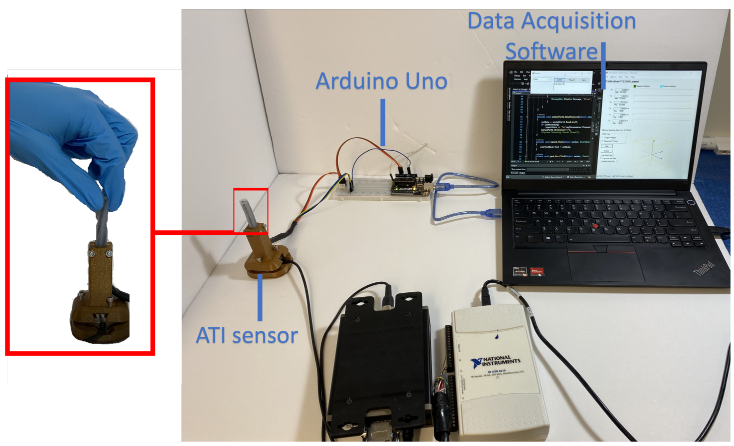

(b)

Figure 4.9: (a) Sensor prototype, (b) Experimental setup for calibration and validation tests.

Table 4.3: Network architectures and hyper-parameters were investigated for the nonlinear calibration of the sensor.

Architectures	Hidden Layers	(2, 4, ...,10)
	Neurons in hidden layer	(10, 25, 50, 100, 250)
Hyper-parameters	Learning rate	(0.1, 0.01, 0.001)
	Optimizer	('*sgd*', '*adam*')
	Activation function	('*ReLU*', '*tanh*')

4.3.2 Feature Selection

The temporal rate of change of sensor outputs has been used in rigid sensors for capturing non-linearities such as rate dependency and hysteresis [101, 91]. We hypothesized that such phenomena might also be present in the current sensor design, given the viscoelastic properties of its components. Thus, for input features of the proposed learning-based model, we selected the input feature vector X as:

$$X = \begin{pmatrix} \frac{V_m}{\hat{V}_m} & \frac{V_e}{\hat{V}_e} & \dot{V}_m & \dot{V}_e \end{pmatrix}^T \tag{26}$$

where $\dot{(.)} = \frac{d}{dt}(.)$ was the temporal derivation operator, and $\hat{V}$ referred to the initial voltages measured before applying any external force. Also, the output vector of the learning-based model Y was:

$$Y = \begin{pmatrix} F_x & F_y & F_z & T_x & T_y & T_z \end{pmatrix}^T \tag{27}$$

Therefore, the input layer had a total of four neurons, and the output layer had a total of six neurons.

4.3.3 Dataset and Training

The sensor prototype depicted in Fig. 4.9(b) was subjected to a series of tip forces and torques manually. Meanwhile, the voltage variations in the sensor were measured using an Arduino Uno. The sensor was serially connected to a 300Ω resistor to build a voltage divider circuit that was bridged to +5v excitation. The sensor's tip was then subjected to forces in three directions: X, Y, and Z. Fig. 4.10 shows th temporal variation of the forces and torques on the setup recorded by the ATI force-torque sensor (reference). Also, Fig. 4.11 depicts the variation of output features with respect to the recorded voltages V_m and V_e.

As shown in Fig. 4.11, in many data points for a given $\begin{pmatrix} V_m V_e \end{pmatrix}$, there might be multiple outputs that indicate the presence of hysteresis. This observation confirms our addition of temporal rates to the features set to distinguish loading and unloading conditions for a given set of voltages.

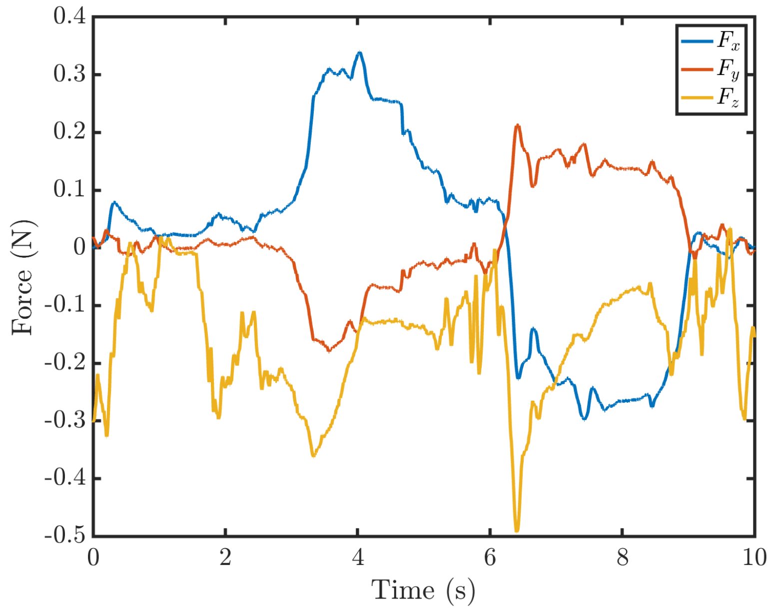

(a)

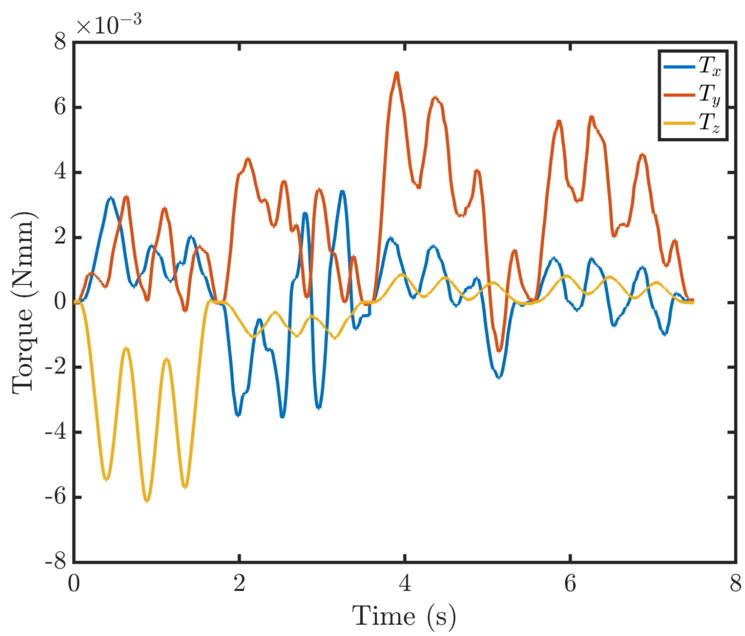

(b)

Figure 4.10: Temporal variation of a representative test for training data used for nonlinear calibration: (a) training forces and (b) training torques.

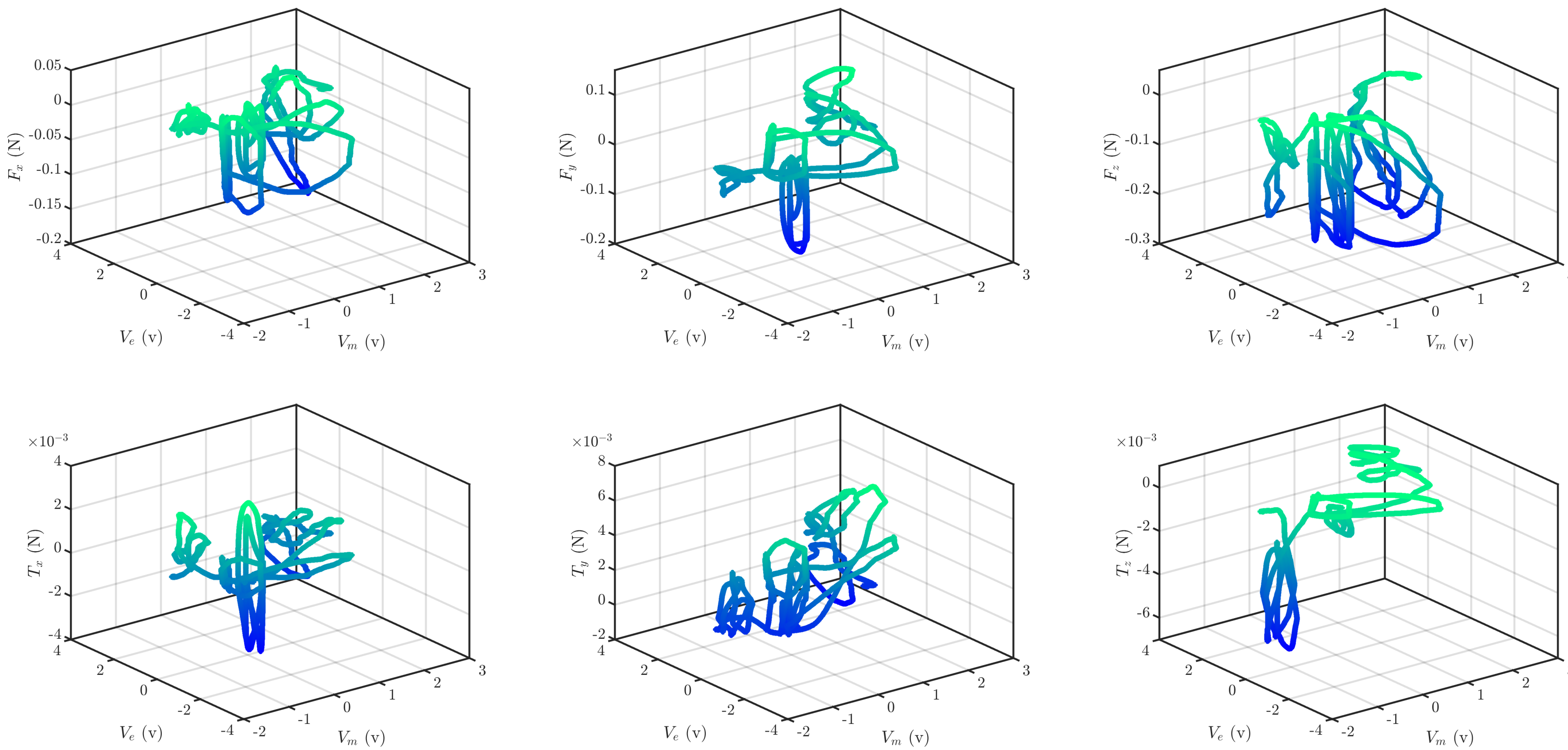

Figure 4.11: Feature-space visualization of the training output used for nonlinear calibration, (a–c) force output and (d –f) torque output.

Table 4.4: Top three best-performing network architectures for calibration model training.

Network	Hidden layers	Learning rate	Optimizer	Activation function	R^2	MAE (N)	RMSE (N)
NN-5.0	(250,150,100,50,10)	0.001	*'adam'*	*'tanh'*	0.98	0.007	0.014
NN-4.0	(250,150,100,50)	0.001	*'adam'*	*'tanh'*	0.93	0.013	0.024
NN-4.1	(250,150,50,10)	0.001	*'adam'*	*'tanh'*	0.90	0.015	0.023

Another observation was that, the recorded force and torques were adequately large to cover the range of motion of the soft body. In other words, the soft body was deformed to its possible extremes while recording the training dataset. In total, five calibration tests were performed and the acquired data were accumulated to create the calibration dataset. In total, 32,441 data samples were acquired from the experiments. The data acquisition tests were not similar in terms of data acquisiton time. Each data sample consisted of two voltages, i.e., V_m and V_e and six reference force torques. The temporal rates of change in the sensor's voltages were calculated *a-posteriori*. To avoid differentiation noise amplification, the raw voltages were filtered using a second-prded Butterworth filter with a cut-off frequency of 25Hz and sample time of 4 ms. The filtered voltages were merely used in rate calculations but not in voltage feature calculations (Eq. 26).

For training the proposed calibration model, the described grid search policy was implemented in Python 3.9 programming language using Scikit-learn 1.1. The dataset was randomly split with a train-to-test ratio of 80:20. Table 4.4 shows the performance of three best-performing network architectures in the grid search. Based on the findings presented in Table 4.4, NN-5.0 model was chosen as the calibration model. Fig. 4.12(a) and (b) show the correlation of predicted forces (F_x, F_y, F_z) and torques (T_x, T_y, T_z) with respect to their ground truth values, respectively. Also, Table 4.5 shows the performance of NN-5.0 in terms of root-mean-square error (RMSE), mean-absolute-error (MAE), and goodness-of-fit (R^2) for predicted forces and torques. The 95% confidence interval (95%CI) was calculated as $\pm 2\sigma$, where σ was the spread (standard-deviation) of the normal distribution fit on the error of prediction of each output (shown in Fig. 4.5). Based on the findings, the worst performance of the calibration model for force prediction was observed for F_z. Nevertheless, the RMSE of F_z prediction was approximately 10 mN with a 95%CI of 20 mN, which is below the required force ranges for applications in the majority of minimally invasive surgeries, i.e., 20 mN [11]. We speculate that the underlying reason for the observed error is that when force was applied

Table 4.5: Performance of NN-5.0 model in calibration of forces and torques on the proposed sensor.

Measurand		RMSE	MAE	R^2	95%CI
Forces	F_x (mN)	4.2	3.3	0.99	8.1
	F_y (mN)	3.5	2.6	0.99	6.8
	F_z (mN)	10.6	8.0	0.96	20.0
Torques	T_x (mNm)	0.17	0.13	0.98	0.32
	T_y (mNm)	0.31	0.24	0.95	0.48
	T_z (mNm)	0.23	0.13	0.93	0.46

along the sensor's z-direction, the sensing element had not experienced significant bending. Thus the changes in resistivity had not been deterministic enough for training the calibration model. This speculation is in agreement with our electro-mechanical model presented in Sec. 4.2.3. Moreover, the minimum detectable values with the proposed sensor were less than 1mN in all axes for force and less than 0.05 mNm in all axes for torques. The exhibited range of measurement with the proposed sensor was (-154 , +30) mN, (-176, 110) mN, and (-284,21) mN for F_x, F_y, and F_z and (-3.7 , 3.4) mNm, (-1.7, 6.8) mNm, and (-6.1,1) mN for T_x, T_y, and T_z. The reason for the asymmetricity of the measurement range may be related to the asymmetricity of the acquired data for training and testing. Since the calibration experiment was performed manually, it was not controlled. Thus, such bias was inevitable. In future studies, a more controlled calibration data acquisition may result in an improved demonstrated measurement range.

4.4 Validation Study

In a separate study, the calibration model was transferred to the developed user interface and was used to predict forces and torques. Meanwhile, the ground truth force and torque values from the ATI sensor were recorded. During the test, the soft body was subjected to manual deformation at its tip in a similar fashion to the training tests. Afterward, the predicted force and torques were compared with the predictions, and the error was analyzed. Fig. 4.13 compares the temporal changes in the predicted and ground truth force and torques in the validation experiment.

The results showed that the predicted forces and torques were in fair agreement; the MAE of forces had an average of 7.4 ± 6.5 mN. Similar to calibration observations, F_z had the largest

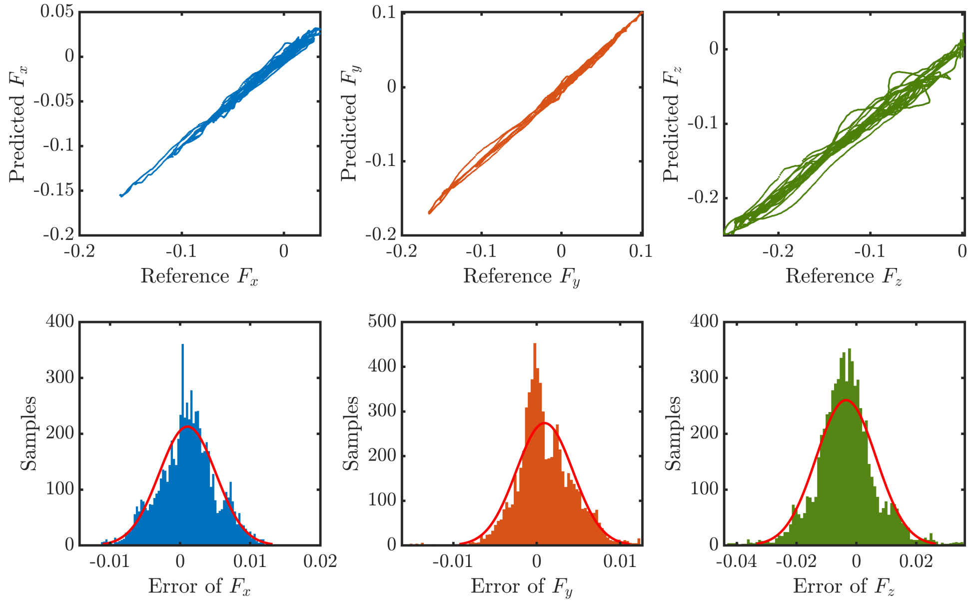

(a)

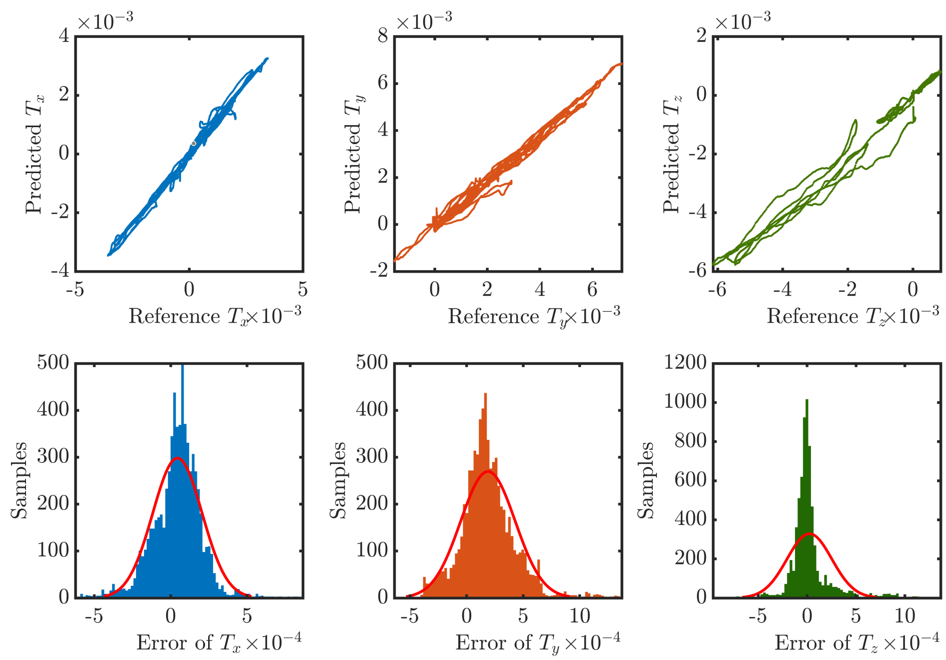

(b)

Figure 4.12: Correlation between calibration model NN-5.0 predictions and ground truth values for (a) forces and (b) torques.

error, i.e., 13 ± 16 mN; nevertheless, its RMSE and MAE remained below the allowable error for minimally invasive procedures. In addition, the computation time for the prediction of force-torques for each sample data was 0.19 ± 0.06 ms on a Mac Studio (128GB RAM, Apple Silicon Ultra CPU) machine. Given the sample rate of the system was 250 Hz, the hardware-software integrated system was well outperforming the real-time requirements (25-30 Hz) for most minimally invasive surgeries. Nevertheless, the performance bottleneck of the integrated system was the sampling rate of Arduino Uno, which can be improved by utilizing a dedicated analog-to-digital converter, e.g., PCI-Express architecture. Given real-time robotic control applications require a refresh rate in the order of kHz, improving the sampling time and refresh rate of the proposed system is of utmost importance for such applications.

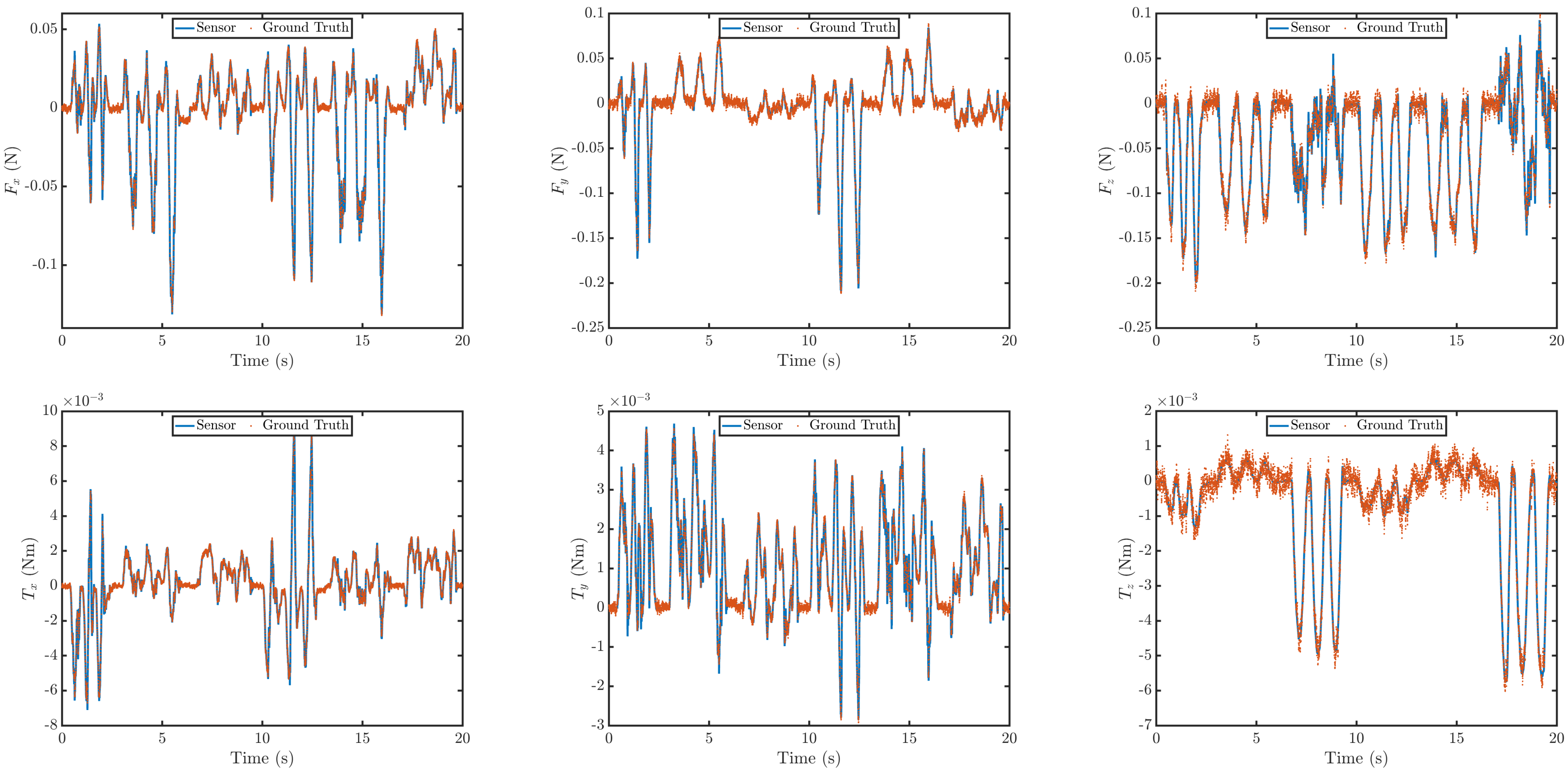

Figure 4.13: Comparison of forces and torques estimated by the proposed sensor versus ground truth.

4.5 Summary

In this study, first, a novel soft sensing element was proposed and modeled. The proposed electro-mechanical model was validated through a comparison of theory with experiment. Afterward, a soft flexural body was fabricated the proposed sensor was embedded in the body. Next, a neural calibration model was selected for the proposed sensor, and its performance in force-torque prediction was investigated. Moreover, the performance of the proposed sensor with neural calibration was demonstrated in experimental validation. The proposed sensor is soft, scalable, and embeddable with soft flexural bodies, e.g., soft robots and minimally invasive surgical instruments. Thus, further fabrication methods and more application-oriented validation studies are required to investigate the proposed sensor's performance. Another expansion of this study can be to calibrate the proposed sensor with shape information, e.g., curvature, so as to be a wearable device for measuring user's finger kinematics, e.g., similar to [118].

Chapter 5

Conclusion and Future Works

5.1 Conclusion

In this thesis, a new class of soft embedded sensors was developed, and three novel sensors were designed, produced, and tested for small-force range applications in soft robotics. The soft sensors proposed were composed of a gelatin-graphite composite having piezoresistive properties. The sensing devices were incorporated directly into the soft flexural structures. For each sensor, a mechano-electrical model for the observed piezoresistance was first constructed and validated. After that, a series of external forces were applied to the sensors to collect calibration data. Given the complexity of piezoresistivity and the significant deformation of soft bodies and sensing elements, a learning-based calibration strategy was studied. In order to correct for rate-dependence and hysteresis effects on sensor readings during calibration, rate-dependent features were chosen for learning-based calibrations. As a result, the initial sensor of this study, a one-degree-of-freedom (1-DoF) force sensor, displayed a force measurement range of 0.035-0.82 N with a mean-absolute-error (MAE) of 3.7% and a resolution of 4.0% of full range. The second sensor, a 3-DoF sensor, had a measurement range of up to 0.3 N, an MAE of 0.005 N, and a resolution of 0.003 N. The third sensor, a 6-DoF force-torque sensor, featured a force range of up to 110 mN with an MAE of 7.4pm6.5 mN and a resolution of 1 mN, as well as a torque range of 6.8 mNm with an MAE of 0.24 mNm. Comparing the proposed sensors to the state-of-the-art and the functional needs of intraluminal procedures revealed that they were compatible with the requirements and improved the state-of-the-art. The most significant contribution of this study was the proposal of a scalable sensing principle that could adapt to the curvature of the host body, such as flexural robots. In addition, this study demonstrated that nonlinear learning-based calibration is a suitable method for overcoming the limits of current soft elastomeric sensor technology.

Based on the author's knowledge, this was the first study to examine the limitations of manufacturing and the complexity of existing technologies for creating piezoresistive sensors. Experimental validation of the proposed sensing principle with nonlinear calibration demonstrated sufficient precision for intraluminal procedures, and a mechano-electrical model of the sensing principle and its validation were performed, enabling future researchers to consider design optimization. One of the significant limitations of this study was the performance of the calibration model for force prediction for F_z. the RMSE of F_z prediction was approximately 10 mN with a 95%CI of 20 mN, which is below the required force ranges for applications in the majority of minimally invasive surgeries, i.e., 20 mN. The underlying cause of the observed error is that when force was applied along the z-axis of the sensor, the sensing element did not experience significant bending. So the changes in resistivity were insufficiently predictable for calibrating the model. Also, the asymmetricity of the acquired data for training and testing may have caused asymmetricity of the measurement range due to the fact that the calibration experiment was performed manually without control; such bias was inevitable.

5.2 Future Studies

To address the limitations of this study, the following suggestions for future studies are provided:

(1) For future studies, a more controlled acquisition of calibration data may result in an enhanced measurement range.

(2) Another improvement is to study the performance of the proposed sensor; more fabrication methods and application-focused validation experiments are needed.

(3) For another extension of this work, the calibration of the suggested sensor with shape information, such as curvature, in order to make it a wearable device for detecting the kinematics

of the user's fingers is suggested.

(4) Investigating other geometry for embedded sensing elements may give better results in terms of enhancing the performance of force in z direction.

(5) Future study may involve integrating the suggested sensor with tendons to enable control systems to manage, command, and direct sensors throughout the body.

Bibliography

[1] Olatunji Mumini Omisore, Shipeng Han, Jing Xiong, Hui Li, Zheng Li, and Lei Wang. A review on flexible robotic systems for minimally invasive surgery. *IEEE Transactions on Systems, Man, and Cybernetics: Systems*, 52(1):631–644, 2022. doi: 10.1109/TSMC.2020.3026174.

[2] E. P.Westebring van der Putten, R. H.M. Goossens, J. J. Jakimowicz, and J. Dankelman. Haptics in minimally invasive surgery - a review. *Minimally Invasive Therapy and Allied Technologies*, 17:3–16, 2008. ISSN 13645706. doi: 10.1080/13645700701820242.

[3] M Tavakoli, RV Patel, and M Moallem. Robotic suturing forces in the presence of haptic feedback and sensory substitution. In *Proceedings of 2005 IEEE Conference on Control Applications, 2005. CCA 2005.*, pages 1–6. IEEE, 2005.

[4] Satyam Kalan, Sanket Chauhan, Rafael F Coelho, Marcelo A Orvieto, Ignacio R Camacho, Kenneth J Palmer, and Vipul R Patel. History of robotic surgery. *Journal of Robotic Surgery*, 4(3):141–147, 2010.

[5] Allison M Okamura. Haptic feedback in robot-assisted minimally invasive surgery. *Current opinion in urology*, 19(1):102, 2009.

[6] Chin-Hsing Kuo and Jian S. Dai. Robotics for minimally invasive surgery: A historical review from the perspective of kinematics. In Hong-Sen Yan and Marco Ceccarelli, editors, *International Symposium on History of Machines and Mechanisms*, pages 337–354, Dordrecht, 2009. Springer Netherlands. ISBN 978-1-4020-9485-9.

[7] Dinesh Vyas and Sean Cronin. Peer review and surgical innovation: robotic surgery and its hurdles. *American journal of robotic surgery*, 2(1):39–44, 2015.

[8] Amir Hooshiar, Masoud Razban, Naghmeh M Bandari, and Javad Dargahi. Sensing principle for real-time characterization of viscoelasticity in the beating myocardial tissue. In *2017 IEEE International Conference on Computational Intelligence and Virtual Environments for Measurement Systems and Applications (CIVEMSA)*, pages 72–77. IEEE, 2017.

[9] Nima Enayati, Elena De Momi, and Giancarlo Ferrigno. Haptics in robot-assisted surgery: Challenges and benefits. *IEEE Reviews in Biomedical Engineering*, 9:49–65, 2016. doi: 10.1109/RBME.2016.2538080.

[10] Ana Luisa Trejos, Abelardo Escoto, Michael D. Naish, and Rajni V. Patel. Design and evaluation of a sterilizable force sensing instrument for minimally invasive surgery. *IEEE Sensors Journal*, 17(13):3983–3993, 2017. doi: 10.1109/JSEN.2017.2703883.

[11] Naghmeh Bandari, Javad Dargahi, and Muthukumaran Packirisamy. Tactile sensors for minimally invasive surgery: a review of the state-of-the-art, applications, and perspectives. *Ieee Access*, 8:7682–7708, 2019.

[12] Chao Huang, Qizhuo Wang, Mingfu Zhao, Chunyan Chen, Sinuo Pan, and Minjie Yuan. Tactile perception technologies and their applications in minimally invasive surgery: A review. *Frontiers in Physiology*, 11, 2020. ISSN 1664-042X. doi: 10.3389/fphys.2020.611596.

[13] Hoseok Song, Heechul Kim, Juwon Jeong, and Jungju Lee. Development of fbg sensor system for force-feedback in minimally invasive robotic surgery. In *2011 Fifth International Conference on Sensing Technology*, pages 16–20. IEEE, 2011.

[14] Uikyum Kim, Dong-Hyuk Lee, Woon Jong Yoon, Blake Hannaford, and Hyouk Ryeol Choi. Force sensor integrated surgical forceps for minimally invasive robotic surgery. *IEEE Transactions on Robotics*, 31(5):1214–1224, 2015. doi: 10.1109/TRO.2015.2473515.

[15] Changhu Lv, Shuxin Wang, and Chaoyang Shi. A high-precision and miniature fiber bragg

grating-based force sensor for tissue palpation during minimally invasive surgery. *Annals of biomedical engineering*, 48(2):669–681, 2020.

[16] Daniele Tosi, Sven Poeggel, Iulian Iordachita, and Emiliano Schena. Fiber optic sensors for biomedical applications. In *Opto-Mechanical Fiber Optic Sensors*, pages 301–333. Elsevier, 2018.

[17] Mário FS Ferreira, Enrique Castro-Camus, David J Ottaway, José Miguel López-Higuera, Xian Feng, Wei Jin, Yoonchan Jeong, Nathalie Picqué, Limin Tong, Björn M Reinhard, et al. Roadmap on optical sensors. *Journal of Optics*, 19(8):083001, 2017.

[18] Frances S Ligler and Chris Rowe Taitt. *Optical biosensors: present & future*. Gulf Professional Publishing, 2002.

[19] Lee CL Chin, William M Whelan, and I Alex Vitkin. Optical fiber sensors for biomedical applications. In *Optical-thermal response of laser-irradiated tissue*, pages 661–712. Springer, 2010.

[20] Kevin Cleary, Andreas Melzer, Vance Watson, Gernot Kronreif, and Dan Stoianovici. Interventional robotic systems: Applications and technology state-of-the-art. *Minimally Invasive Therapy & Allied Technologies*, 15(2):101–113, 2006.

[21] Pinyo Puangmali, Kaspar Althoefer, Lakmal D. Seneviratne, Declan Murphy, and Prokar Dasgupta. State-of-the-art in force and tactile sensing for minimally invasive surgery. *IEEE Sensors Journal*, 8(4):371–381, 2008. doi: 10.1109/JSEN.2008.917481.

[22] Weiqiang Dou, Guoliang Zhong, Jinglin Cao, Zhun Shi, Bowen Peng, and Liangzhong Jiang. Soft robotic manipulators: Designs, actuation, stiffness tuning, and sensing. *Advanced Materials Technologies*, 6(9):2100018, 2021. doi: https://doi.org/10.1002/admt.202100018.

[23] Chunfeng Wang, Lin Dong, Dengfeng Peng, and Caofeng Pan. Tactile sensors for advanced intelligent systems. *Advanced Intelligent Systems*, 1(8):1900090, 2019. doi: https://doi.org/10.1002/aisy.201900090.

[24] Ahmed Salim and Sungjoon Lim. Review of recent inkjet-printed capacitive tactile sensors. *Sensors*, 17(11), 2017. ISSN 1424-8220. doi: 10.3390/s17112593.

[25] Issam El Rassi and Jean-Michel El Rassi. A review of haptic feedback in tele-operated robotic surgery. *Journal of medical engineering & technology*, 44(5):247–254, 2020.

[26] Soonjae Pyo, Jaeyong Lee, Kyubin Bae, Sangjun Sim, and Jongbaeg Kim. Recent progress in flexible tactile sensors for human-interactive systems: from sensors to advanced applications. *Advanced Materials*, 33(47):2005902, 2021.

[27] Jagoda Anna Dobrzynska and MAM Gijs. Polymer-based flexible capacitive sensor for three-axial force measurements. *Journal of Micromechanics and Microengineering*, 23(1):015009, 2012.

[28] Harshal Arun Sonar and Jamie Paik. Soft pneumatic actuator skin with piezoelectric sensors for vibrotactile feedback. *Frontiers in Robotics and AI*, 2:38, 2016.

[29] Hongbo Wang, Massimo Totaro, and Lucia Beccai. Toward perceptive soft robots: Progress and challenges. *Advanced Science*, 5(9):1800541, 2018.

[30] Siamak Najarian, Javad Dargahi, and Ali Abouei Mehrizi. *Artificial tactile sensing in biomedical engineering*. McGraw-Hill Education, 2009.

[31] Stefania Russo, Tommaso Ranzani, Hongbin Liu, Samia Nefti-Meziani, Kaspar Althoefer, and Arianna Menciassi. Soft and stretchable sensor using biocompatible electrodes and liquid for medical applications. *Soft Robotics*, 2:146–154, 12 2015. ISSN 21695180. doi: 10.1089/soro.2015.0011.

[32] Naghmeh Bandari, Javad Dargahi, and Muthukumaran Packirisamy. Tactile sensors for minimally invasive surgery: A review of the state-of-the-art, applications, and perspectives. *IEEE Access*, 8:7682–7708, 2020. ISSN 21693536. doi: 10.1109/ACCESS.2019.2962636.

[33] M. Tanimoto, F. Arai, T. Fukuda, H. Iwata, K. Itoigawa, Y. Gotoh, M. Hashimoto, and M. Negoro. Micro force sensor for intravascular neurosurgery and in vivo experiment. In *Proceedings MEMS 98. IEEE. Eleventh Annual International Workshop on Micro Electro Mechanical Systems. An Investigation of Micro Structures, Sensors, Actuators, Machines and Systems (Cat. No.98CH36176*, pages 504–509, 1998. doi: 10.1109/MEMSYS.1998.659809.

[34] J. Dargahi and S. Najarian. An endoscopic force-position sensor grasper with minimum sensors. *Canadian Journal of Electrical and Computer Engineering*, 28(3/4):155–161, 2003. doi: 10.1109/CJECE.2003.1425102.

[35] Apu Sarmah and U. D. Gulhane. Surgical robot teleoperated laparoscopic grasper with haptics feedback system. In *INTERACT-2010*, pages 288–291, 2010. doi: 10.1109/INTERACT.2010.5706162.

[36] Chih-Hung King, Martin O. Culjat, Miguel L. Franco, Catherine E. Lewis, Erik P. Dutson, Warren S. Grundfest, and James W. Bisley. Tactile feedback induces reduced grasping force in robot-assisted surgery. *IEEE Transactions on Haptics*, 2(2):103–110, 2009. doi: 10.1109/TOH.2009.4.

[37] Masoud Kalantari, Mohammadreza Ramezanifard, Roozbeh Ahmadi, Javad Dargahi, and József Kövecses. A piezoresistive tactile sensor for tissue characterization during catheter-based cardiac surgery. *The International Journal of Medical Robotics and Computer Assisted Surgery*, 7(4):431–440, 2011.

[38] Hongbo Wang, Massimo Totaro, and Lucia Beccai. Toward perceptive soft robots: Progress and challenges. *Advanced Science*, 5, 9 2018. ISSN 21983844. doi: 10.1002/advs.201800541.

[39] Yong-Lae Park, Bor-Rong Chen, and Robert J. Wood. Design and fabrication of soft artificial skin using embedded microchannels and liquid conductors. *IEEE Sensors Journal*, 12(8): 2711–2718, Aug 2012. ISSN 1558-1748. doi: 10.1109/JSEN.2012.2200790.

[40] Amar M Kamat, Yutao Pei, Bayu Jayawardhana, and Ajay Giri Prakash Kottapalli.

Biomimetic soft polymer microstructures and piezoresistive graphene mems sensors using sacrificial metal 3d printing. *ACS applied materials & interfaces*, 13(1):1094–1104, 2021.

[41] Panagiotis Polygerinos, Nikolaus Correll, Stephen A Morin, Bobak Mosadegh, Cagdas D Onal, Kirstin Petersen, Matteo Cianchetti, Michael T Tolley, and Robert F Shepherd. Soft robotics: Review of fluid-driven intrinsically soft devices; manufacturing, sensing, control, and applications in human-robot interaction. *Advanced Engineering Materials*, 19(12): 1700016, 2017.

[42] Tim Helps and Jonathan Rossiter. Proprioceptive flexible fluidic actuators using conductive working fluids. *Soft Robotics*, 5(2):175–189, 2018. doi: 10.1089/soro.2017.0012. PMID: 29211627.

[43] Jean-Baptiste Chossat, Yong-Lae Park, Robert J Wood, and Vincent Duchaine. A soft strain sensor based on ionic and metal liquids. *Ieee sensors journal*, 13(9):3405–3414, 2013.

[44] Meital Segev-Bar and Hossam Haick. Flexible sensors based on nanoparticles. *ACS nano*, 7 (10):8366–8378, 2013.

[45] Jongyoun Kim, Hyeonwoo Jung, Minkyoung Kim, Hyejeong Bae, and Youngu Lee. Conductive polymer composites for soft tactile sensors. *Macromolecular Research*, 29(11):761–775, 2021.

[46] Takeo Yamada, Yuhei Hayamizu, Yuki Yamamoto, Yoshiki Yomogida, Ali Izadi-Najafabadi, Don N Futaba, and Kenji Hata. A stretchable carbon nanotube strain sensor for human-motion detection. *Nature nanotechnology*, 6(5):296–301, 2011.

[47] Zhenhua Tang, Shuhai Jia, Si Shi, Fei Wang, and Bo Li. Coaxial carbon nanotube/polymer fibers as wearable piezoresistive sensors. *Sensors and Actuators A: Physical*, 284:85–95, 2018. ISSN 0924-4247. doi: https://doi.org/10.1016/j.sna.2018.10.012.

[48] Zhenhua Tang, Shuhai Jia, Xuesong Shi, Bo Li, and Chenghao Zhou. Coaxial printing of silicone elastomer composite fibers for stretchable and wearable piezoresistive sensors. *Polymers*, 11(4), 2019. ISSN 2073-4360. doi: 10.3390/polym11040666.

[49] Ying Yi, Ayman Samara, and Bo Wang. A new approach for an ultra-thin piezoresistive sensor based on solidified carbon ink film. *Journal of Materials Science*, 56(1):607–614, 2021.

[50] Amir Firouzeh, Antoine Foba Amon-Junior, and Jamie Paik. Soft piezoresistive sensor model and characterization with varying design parameters. *Sensors and Actuators A: Physical*, 233: 158–168, 2015. ISSN 0924-4247. doi: https://doi.org/10.1016/j.sna.2015.06.007.

[51] Hong Seok Jo, Seongpil An, Chan-Woo Park, Deok-Yoon Woo, Alexander L Yarin, and Sam S Yoon. Wearable, stretchable, transparent all-in-one soft sensor formed from supersonically sprayed silver nanowires. *ACS applied materials & interfaces*, 11(43):40232–40242, 2019.

[52] Yin Cheng, Shouling Wang, Ranran Wang, Jing Sun, and Lian Gao. Copper nanowire based transparent conductive films with high stability and superior stretchability. *Journal of Materials Chemistry C*, 2(27):5309–5316, 2014.

[53] Tian-Ling Ren, He Tian, Dan Xie, and Yi Yang. Flexible graphite-on-paper piezoresistive sensors. *Sensors*, 12(5):6685–6694, 2012.

[54] Kai-Yue Chen, Yun-Ting Xu, Yang Zhao, Jun-Kai Li, Xiao-Peng Wang, and Liang-Ti Qu. Recent progress in graphene-based wearable piezoresistive sensors: From 1d to 3d device geometries. *Nano Materials Science*, In-press, 2022. ISSN 2589-9651. doi: https://doi.org/10.1016/j.nanoms.2021.11.003.

[55] Hairong Kou, Lei Zhang, Qiulin Tan, Guanyu Liu, Helei Dong, Wendong Zhang, and Jijun Xiong. Wireless wide-range pressure sensor based on graphene/pdms sponge for tactile monitoring. *Scientific reports*, 9(1):1–7, 2019.

[56] Hao Wang, Zifen Zhao, Panpan Liu, and Xiaogang Guo. A soft and stretchable electronics using laser-induced graphene on polyimide/pdms composite substrate. *npj Flexible Electronics*, 6(1):1–10, 2022.

[57] Chaoyi Yan, Jiangxin Wang, and Pooi See Lee. Stretchable graphene thermistor with tunable thermal index. *ACS nano*, 9(2):2130–2137, 2015.

[58] Urte Samukaite Bubniene, Vilma Ratautaite, Arunas Ramanavicius, and Vytautas Bucinskas. Conducting polymers for the design of tactile sensors. *Polymers*, 14(15), 2022. ISSN 2073-4360. doi: 10.3390/polym14152984.

[59] Sree Lakshmi Kanuri. *Fabrication, characterization and evaluation of graphite-polyvinyl alcohol based piezoresistive sensors*. PhD thesis, The Florida State University, 2013.

[60] Li Tang, Shaoji Wu, Jie Qu, Liang Gong, and Jianxin Tang. A review of conductive hydrogel used in flexible strain sensor. *Materials*, 13(18), 2020. ISSN 1996-1944. doi: 10.3390/ma13183947.

[61] Kai Ren, Yu Cheng, Chao Huang, Rui Chen, Zhao Wang, and Jie Wei. Self-healing conductive hydrogels based on alginate, gelatin and polypyrrole serve as a repairable circuit and a mechanical sensor. *Journal of Materials Chemistry B*, 7(37):5704–5712, 2019.

[62] Sushmitha Veeralingam and Sushmee Badhulika. Low-density, stretchable, adhesive pvdf-polypyrrole reinforced gelatin based organohydrogel for uv photodetection, tactile and strain sensing applications. *Materials Research Bulletin*, 150:111779, 2022. ISSN 0025-5408. doi: https://doi.org/10.1016/j.materresbull.2022.111779.

[63] David Hardman, Thomas George Thuruthel, and Fumiya Iida. Self-healing ionic gelatin/glycerol hydrogels for strain sensing applications. *NPG Asia Materials*, 14(1):1–13, 2022.

[64] Xuechuan Wang, Zhongxue Bai, Manhui Zheng, Ouyang Yue, Mengdi Hou, Boqiang Cui, Rongrong Su, Chao Wei, and Xinhua Liu. Engineered gelatin-based conductive hydrogels for flexible wearable electronic devices: Fundamentals and recent advances. *Journal of Science: Advanced Materials and Devices*, 7(3):100451, 2022. ISSN 2468-2179. doi: https://doi.org/10.1016/j.jsamd.2022.100451.

[65] Yi-Zhou Zhang, Kang Hyuck Lee, Dalaver H Anjum, Rachid Sougrat, Qiu Jiang, Hyunho Kim, and Husam N Alshareef. Mxenes stretch hydrogel sensor performance to new limits. *Science advances*, 4(6):eaat0098, 2018.

[66] Yichen Cai, Jie Shen, Gang Ge, Yizhou Zhang, Wanqin Jin, Wei Huang, Jinjun Shao, Jian Yang, and Xiaochen Dong. Stretchable ti3c2tx mxene/carbon nanotube composite based strain sensor with ultrahigh sensitivity and tunable sensing range. *ACS Nano*, 12(1):56–62, 2018. doi: 10.1021/acsnano.7b06251. PMID: 29202226.

[67] Li-Yin Hsiao, Lin Jing, Kerui Li, Haitao Yang, Yang Li, and Po-Yen Chen. Carbon nanotube-integrated conductive hydrogels as multifunctional robotic skin. *Carbon*, 161:784–793, 2020. ISSN 0008-6223. doi: https://doi.org/10.1016/j.carbon.2020.01.109.

[68] Jui-Chi Lin, Panos Liatsis, and Paschalis Alexandridis. Flexible and stretchable electrically conductive polymer materials for physical sensing applications. *Polymer Reviews*, pages 1–60, 2022.

[69] Moinuddin Ahmed, Murali M. Chitteboyina, Donald P. Butler, and Zeynep Çelik Butler. Mems force sensor in a flexible substrate using nichrome piezoresistors. *IEEE Sensors Journal*, 13(10):4081–4089, 2013. doi: 10.1109/JSEN.2013.2272881.

[70] Yanan Ma, Nishuang Liu, Luying Li, Xiaokang Hu, Zhengguang Zou, Jianbo Wang, Shijun Luo, and Yihua Gao. A highly flexible and sensitive piezoresistive sensor based on mxene with greatly changed interlayer distances. *Nature communications*, 8(1):1–8, 2017.

[71] Minxuan Xu, Feng Li, Zhenyun Zhang, Tao Shen, Qian Zhang, and Junjie Qi. Stretchable and multifunctional strain sensors based on 3d graphene foams for active and adaptive tactile imaging. *Science China Materials*, 62(4):555–565, 2019.

[72] Hu Liu, Mengyao Dong, Wenju Huang, Jiachen Gao, Kun Dai, Jiang Guo, Guoqiang Zheng, Chuntai Liu, Changyu Shen, and Zhanhu Guo. Lightweight conductive graphene/thermoplastic polyurethane foams with ultrahigh compressibility for piezoresistive sensing. *Journal of Materials Chemistry C*, 5(1):73–83, 2017.

[73] Conor S. Boland, Umar Khan, Gavin Ryan, Sebastian Barwich, Romina Charifou, Andrew Harvey, Claudia Backes, Zheling Li, Mauro S. Ferreira, Matthias E. Möbius, Robert J. Young, and Jonathan N. Coleman. Sensitive electromechanical sensors using viscoelastic graphene-polymer nanocomposites. *Science*, 354(6317):1257–1260, 2016. doi: 10.1126/science.aag2879.

[74] Jin Jia, Guotao Huang, Jianping Deng, and Kai Pan. Skin-inspired flexible and high-sensitivity pressure sensors based on rgo films with continuous-gradient wrinkles. *Nanoscale*, 11(10):4258–4266, 2019.

[75] Tingting Zhao, Tongkuai Li, Longlong Chen, Li Yuan, Xifeng Li, and Jianhua Zhang. Highly sensitive flexible piezoresistive pressure sensor developed using biomimetically textured porous materials. *ACS applied materials & interfaces*, 11(32):29466–29473, 2019.

[76] Chanhyuk Lim, Yoonsoo Shin, Jaebong Jung, Ji Hoon Kim, Sangkyu Lee, and Dae-Hyeong Kim. Stretchable conductive nanocomposite based on alginate hydrogel and silver nanowires for wearable electronics. *APL Materials*, 7(3):031502, 2018.

[77] Yuhua Zhang. Sensitivity enhancement of a micro-scale biomimetic tactile sensor with epidermal ridges. *Journal of micromechanics and microengineering*, 20(8):085012, 2010.

[78] Uday Tata, Hung Cao, Vaibhav Landge, Cuong M Nguyen, Young-Sik Seo, and J-C Chiao. Wireless strain sensor based on amorphous carbon for human-motion detection. In *2013 IEEE Topical Conference on Biomedical Wireless Technologies, Networks, and Sensing Systems*, pages 31–33. IEEE, 2013.

[79] Xu Liu, Dan Liu, Jeng-hun Lee, Qingbin Zheng, Xiaohan Du, Xinyue Zhang, Hongru Xu, Zhenyu Wang, Ying Wu, Xi Shen, et al. Spider-web-inspired stretchable graphene woven fabric for highly sensitive, transparent, wearable strain sensors. *ACS applied materials & interfaces*, 11(2):2282–2294, 2018.

[80] Qingbin Zheng, Jeng-hun Lee, Xi Shen, Xiaodong Chen, and Jang-Kyo Kim. Graphene-based wearable piezoresistive physical sensors. *Materials Today*, 36:158–179, 2020.

[81] Qingbin Zheng, Zhigang Li, Junhe Yang, and Jang-Kyo Kim. Graphene oxide-based transparent conductive films. *Progress in Materials Science*, 64:200–247, 2014. ISSN 0079-6425. doi: https://doi.org/10.1016/j.pmatsci.2014.03.004.

[82] Wanasinghe Arachchige Dumith Madushanka Jayathilaka, Kun Qi, Yanli Qin, Amutha Chinnappan, William Serrano-García, Chinnappan Baskar, Hongbo Wang, Jianxin He, Shizhong Cui, Sylvia W Thomas, et al. Significance of nanomaterials in wearables: a review on wearable actuators and sensors. *Advanced Materials*, 31(7):1805921, 2019.

[83] Balamurugan Thirumalraj, Rajalakshmi Sakthivel, Shen-Ming Chen, Chellakannu Rajkumar, Lin-kuan Yu, and Subbiramaniyan Kubendhiran. A reliable electrochemical sensor for determination of h2o2 in biological samples using platinum nanoparticles supported graphite/gelatin hydrogel. *Microchemical Journal*, 146:673–678, 2019.

[84] Rajalakshmi Sakthivel, Selvakumar Palanisamy, Shen-Ming Chen, Sukanya Ramaraj, Vijayalakshmi Velusamy, Pan Yi-Fan, James M Hall, and Sayee Kannan Ramaraj. A robust nitrobenzene electrochemical sensor based on chitin hydrogel entrapped graphite composite. *Journal of the Taiwan Institute of Chemical Engineers*, 80:663–668, 2017.

[85] Nabarun Roy, Bernd Bruchmann, and Jean-Marie Lehn. Dynamers: dynamic polymers as self-healing materials. *Chemical Society Reviews*, 44(11):3786–3807, 2015.

[86] Eleonora D'Elia, Suelen Barg, Na Ni, Victoria G. Rocha, and Eduardo Saiz. Self-healing graphene-based composites with sensing capabilities. *Advanced Materials*, 27(32):4788–4794, 2015. doi: https://doi.org/10.1002/adma.201501653.

[87] Dong Hae Ho, Qijun Sun, So Young Kim, Joong Tark Han, Do Hwan Kim, and Jeong Ho Cho. Stretchable and multimodal all graphene electronic skin. *Advanced Materials*, 28(13): 2601–2608, 2016.

[88] Heng Zhang, Dan Liu, Jeng-Hun Lee, Haomin Chen, Eunyoung Kim, Xi Shen, Qingbin Zheng, Jinglei Yang, and Jang-Kyo Kim. Anisotropic, wrinkled, and crack-bridging structure for ultrasensitive, highly selective multidirectional strain sensors. *Nano-micro letters*, 13(1): 1–15, 2021.

[89] Shuang Huang, Gen He, Cheng Yang, Jiangming Wu, Chan Guo, Tian Hang, Baohong Li, Chengduan Yang, Di Liu, Hui-Jiuan Chen, et al. Stretchable strain vector sensor based on parallelly aligned vertical graphene. *ACS applied materials & interfaces*, 11(1):1294–1302, 2018.

[90] Tran Thanh Tung, Jeongha Yoo, Faisal K Alotaibi, Md J Nine, Ramesh Karunagaran, Melinda Krebsz, Giang T Nguyen, Diana NH Tran, Jean-Francois Feller, and Dusan Losic. Graphene oxide-assisted liquid phase exfoliation of graphite into graphene for highly conductive film and electromechanical sensors. *ACS applied materials & interfaces*, 8(25):16521–16532, 2016.

[91] Tannaz Torkaman, Majid Roshanfar, Javad Dargahi, and Amir Hooshiar. Analytical modeling and experimental validation of a gelatin-based shape sensor for soft robots. In *2022 International Symposium on Medical Robotics (ISMR)*, pages 1–7. IEEE, 2022.

[92] Yong-Lae Park, Bor-Rong Chen, and Robert J. Wood. Design and fabrication of soft artificial skin using embedded microchannels and liquid conductors. *IEEE Sensors Journal*, 12(8): 2711–2718, 2012. doi: 10.1109/JSEN.2012.2200790.

[93] Tim Helps and Jonathan Rossiter. Proprioceptive flexible fluidic actuators using conductive working fluids. *Soft Robotics*, 5(2):175–189, 2018. doi: 10.1089/soro.2017.0012. PMID: 29211627.

[94] Min Pan, Chenggang Yuan, Hastha Anpalagan, Andrew Plummer, Jun Zou, Junhui Zhang, and Chris Bowen. Soft controllable carbon fibre-based piezoresistive self-sensing actuators. *Actuators*, 9(3), 2020. ISSN 2076-0825. doi: 10.3390/act9030079.

[95] Manhui Zheng, Xuechuan Wang, Ouyang Yue, Mengdi Hou, Huijie Zhang, Sebastian Beyer, Anna Maria Blocki, Qin Wang, Guidong Gong, Xinhua Liu, et al. Skin-inspired gelatin-based flexible bio-electronic hydrogel for wound healing promotion and motion sensing. *Biomaterials*, 276:121026, 2021.

[96] Zhipeng Yang, Hongqiang Li, Chengkai Li, Xuejun Lai, and Xingrong Zeng. Conductive

and room-temperature self-healable polydimethylsiloxane-based elastomer film with ridge-like microstructure for piezoresistive pressure sensor. *Chemical Engineering Journal*, 430: 133103, 2022.

[97] Weiwei Zhao, Zhijun Shi, Sanming Hu, Guang Yang, and Huifang Tian. Understanding piezoelectric characteristics of phema-based hydrogel nanocomposites as soft self-powered electronics. *Advanced Composites and Hybrid Materials*, 1(2):320–331, 2018.

[98] Jie Wang, Fu Tang, Yue Wang, Qipeng Lu, Shuqi Liu, and Lidong Li. Self-healing and highly stretchable gelatin hydrogel for self-powered strain sensor. *ACS Applied Materials & Interfaces*, 12(1):1558–1566, 2020. doi: 10.1021/acsami.9b18646. PMID: 31808668.

[99] Panupong Jaipan, Alexander Nguyen, and Roger J Narayan. Gelatin-based hydrogels for biomedical applications. *Mrs Communications*, 7(3):416–426, 2017.

[100] Amir Hooshiar, Siamak Najarian, and Javad Dargahi. Haptic telerobotic cardiovascular intervention: a review of approaches, methods, and future perspectives. *IEEE reviews in biomedical engineering*, 13:32–50, 2019.

[101] Naghmeh Bandari, Javad Dargahi, and Muthukumaran Packirisamy. Miniaturized optical force sensor for minimally invasive surgery with learning-based nonlinear calibration. *IEEE Sensors Journal*, 20(7):3579–3592, 2019.

[102] Mohammad Jolaei, Amir Hooshiar, Javad Dargahi, and Muthukumaran Packirisamy. Toward task autonomy in robotic cardiac ablation: Learning-based kinematic control of soft tendon-driven catheters. *Soft Robotics*, 8(3):340–351, 2021.

[103] Chia-Wen Tsao. Polymer microfluidics: Simple, low-cost fabrication process bridging academic lab research to commercialized production. *Micromachines*, 7(12):225, 2016.

[104] Mohammad Jolaei, Amir Hooshiar, and Javad Dargahi. Displacement-based model for estimation of contact force between rfa catheter and atrial tissue with ex-vivo validation. In *2019 IEEE International Symposium on Robotic and Sensors Environments (ROSE)*, pages 1–7. IEEE, 2019.

[105] Mohammad Jolaei, Amir Hooshiar, Amir Sayadi, Javad Dargahi, and Muthukumaran Packirisamy. Sensor-free force control of tendon-driven ablation catheters through position control and contact modeling. In *2020 42nd Annual International Conference of the IEEE Engineering in Medicine & Biology Society (EMBC)*, pages 5248–5251. IEEE, 2020.

[106] ISO 7743. Rubber, vulcanized or thermoplastic — Determination of compression stress-strain properties, 2017.

[107] Eric J Markvicka, Michael D Bartlett, Xiaonan Huang, and Carmel Majidi. An autonomously electrically self-healing liquid metal–elastomer composite for robust soft-matter robotics and electronics. *Nature materials*, 17(7):618–624, 2018.

[108] Yang Yang and Zhiqun Daniel Deng. Stretchable sensors for environmental monitoring. *Applied Physics Reviews*, 6(1):011309, 2019.

[109] Weiqiang Dou, Guoliang Zhong, Jinglin Cao, Zhun Shi, Bowen Peng, and Liangzhong Jiang. Soft robotic manipulators: Designs, actuation, stiffness tuning, and sensing. *Wiley Online Library*, 6(9), sep 2021. doi: 10.1002/admt.202100018.

[110] M Jolaei, A Hooshiar, J Dargahi, M Packirisamy Soft Robotics, and undefined 2021. Toward task autonomy in robotic cardiac ablation: Learning-based kinematic control of soft tendon-driven catheters. *liebertpub.com*, 8(3):340–351, jun 2021. doi: 10.1089/soro.2020.0006.

[111] Mohammad Jolaei, Amir Hooshiar, and Javad Dargahi. Displacement-based model for estimation of contact force between RFA catheter and atrial tissue with ex-vivo validation. *IEEE International Symposium on Robotic and Sensors Environments, ROSE 2019 - Proceedings*, jun 2019. doi: 10.1109/ROSE.2019.8790415.

[112] AS Fiorillo, CD Critello, and SA Pullano. Theory, technology and applications of piezoresistive sensors: A review. *Sensors and Actuators A: Physical*, 281:156–175, 2018.

[113] Yuan Zhu, Yang Liu, Yunna Sun, Yanxin Zhang, and Guifu Ding. Recent advances in resistive sensor technology for tactile perception: A review. *IEEE Sensors Journal*, 22(16):15635–15649, 2022. doi: 10.1109/JSEN.2022.3179015.

[114] Jiaqi Zhu, Liangxiong Lyu, Yi Xu, Huageng Liang, Xiaoping Zhang, Han Ding, and Zhigang Wu. Intelligent soft surgical robots for next-generation minimally invasive surgery. *Advanced Intelligent Systems*, 3(5):2100011, 2021. doi: https://doi.org/10.1002/aisy.202100011.

[115] Daniela Rus and Michael T Tolley. Design, fabrication and control of soft robots. *Nature*, 521(7553):467–475, 2015.

[116] Justina Vaicekauskaite, Piotr Mazurek, Sindhu Vudayagiri, and Anne Ladegaard Skov. Silicone elastomer map: design the ideal elastomer. In *Electroactive Polymer Actuators and Devices (EAPAD) XXI*, volume 10966, pages 297–305. SPIE, 2019.

[117] Stefania Russo, Tommaso Ranzani, Hongbin Liu, Samia Nefti-Meziani, Kaspar Althoefer, and Arianna Menciassi. Soft and stretchable sensor using biocompatible electrodes and liquid for medical applications. *Soft robotics*, 2(4):146–154, 2015.

[118] Amir Hooshiar, Amir Sayadi, Javad Dargahi, and Siamak Najarian. Integral-free spatial orientation estimation method and wearable rotation measurement device for robot-assisted catheter intervention. *IEEE/ASME Transactions on Mechatronics*, 27(2):766–776, 2021.